fluids

Article

Solid–Liquid Flow Analysis Using Simultaneous Two-Phase PIV in a Stirred Tank Bioreactor

Mohamad Madani *, Angélique Delafosse, Sébastien Calvo and Dominique Toye

Department of Chemical Engineering, Product, Environment and Processes PEPs, University of Liege, 4000 Liege, Belgium; scalvo@uliege.be (S.C.); dominique.toye@uliege.be (D.T.)
* Correspondence: m.madani@uliege.be

Abstract

Solid–liquid stirred tanks are widely used in multiphase processes, including bioreactors for mesenchymal stem cell (MSC) culture, yet simultaneous experimental data for both dispersed and carrier phases remain limited. Here, a refractive index-matched (RIM) suspension of PMMA microparticles ($d_p = 168\,\mu\text{m}$, $\rho_p/\rho_l \approx 0.96$) in an NH_4SCN solution is studied at an intermediate Reynolds number ($Re \approx 5000$), low Stokes number ($St = 0.078$), and particle volume fractions $0.1 \leq \alpha_p \leq 0.5\,\text{v\%}$. This system was previously established and studied for the effect of addition of particles on the carrier phase. In this work, a dual-camera PIV set-up provides simultaneous velocity fields of the liquid and particle phases in a stirred tank equipped with a three-blade down-pumping HTPGD impeller. The liquid mean flow and circulation loop remained essentially unchanged with particle loading, whereas particle mean velocities were lower than single-phase and liquid-phase values in the impeller discharge. Turbulence levels diverged between phases: liquid-phase turbulent kinetic energy (TKE) in the impeller region increased modestly with α_p, while solid-phase TKE was attenuated. Slip velocity maps showed that particles lagged the fluid in the impeller jet and deviated faster from the wall in the upward flow, with slip magnitudes increasing with α_p. An approximate axial force balance indicated that drag dominates over lift in the impeller and wall regions, while the balance is approximately satisfied in the tank bulk, providing an experimental benchmark for refining drag and lift models in this class of stirred tanks.

Keywords: solid-liquid flow; two-phase PIV; stirred tank; slip velocity; mixing; mesenchymal stem cells

Check for updates

Academic Editors: Van-Tu Nguyen, Hemant J. Sagar and Jun Yao

Received: 25 November 2025
Revised: 20 December 2025
Accepted: 4 January 2026
Published: 8 January 2026

1. Introduction

Multiphase flows occur in nature and in an abundance of industrial processes, such as aerospace [1], metallurgy [2], and chemical engineering. Within the world of chemical engineering, examples include crude oil recovery [3], catalysts in chemical reactors [4], and food production [5]. Dispersed multiphase systems consist of small particles, bubbles, or droplets that are suspended in a continuous medium. The continuous phase generally acts as a carrier, often demonstrating turbulent flow, while the dispersed phase can influence the behavior of this carrier flow [6].

The presence of a dispersed phase in a continuous carrier flow adds challenges to the experimental characterization, which is essential to understand the interactions between both phases. The interactions would affect the properties and behavior of the discrete/dispersed phase and those of the carrier flow. The impacts include alterations on

https://doi.org/10.3390/fluids11010017

local flow velocities, local volume fractions distribution of rigid particles, size distribution of droplets/bubbles, and local residence time of dispersed phases. The presence of the dispersed phase could also introduce particle–particle interactions as well as coalescence–rupture of bubbles/droplets that add complexities to the flow. Other impacts on system performance could be on the global scheme of things, such as mass and heat transfer rates and power consumption. Over the years, researchers have developed and tested computational tools to model interfacial phenomena and interactions [7,8]. However, to validate the numerical tools and inspire the principal models, recording and collecting experimental data are a must. Hence, in all cases, developing experimental techniques is essential to inspect and optimize the process. Several measurement techniques, in addition to modeling approaches, have been established and documented [6,9].

Experimental techniques for multiphase flows include intrusive probes such as hot-wire anemometry and electrical impedance probes, which can provide local measurements of interfaces, void fractions and phase velocities, and can be extended to wire-mesh sensors for 2D/3D mapping, but the invasive nature disturbs interfaces and particle paths, which leads to biased errors [10–17]. Nonintrusive imaging methods like shadowgraphy offer backlit volumetric illumination with effectively infinite depth of field and are well suited for sizing and 3D tracking in dilute systems, but require long optical benches and are limited by depth-of-field effects, since objects outside the focal region appear blurred and affect statistics [18–22]. Additionally, tomographic approaches (X-Ray, γ-Ray and electrical tomography) are used to reconstruct cross-sectional phase distributions from peripheral measurements, but such techniques are limited to high cost, safety constraints, and reconstruction algorithms [23–31]. As tomography mainly yields phase-distribution maps, detailed hydrodynamics are typically captured with laser-based methods such as PIV and PTV, which measure dispersed and carrier-phase velocities using light scattering or fluorescence and rely on phase discrimination through image processing, wavelength-based separation or correlation analysis. These techniques have been successfully applied to a variety of multiphase configurations, including pipe flows, open channels, jets, sprays, grid turbulence and stirred tanks [32–40]. A more consolidated review of the developments of experimental techniques for multiphase flows is provided by Villafañe et al. [41].

Stirred tanks have been numerously investigated so far, but the turbulent characteristics of the multiphase flow inside the tank are still open for debate [42]. A typical flow type is a solid–liquid one where particles of different sizes are suspended inside the tank. Only few studies were conducted to simultaneously measure the dispersed and carrier phases in stirred tanks via PIV. Most studies focused on the effect of the dispersed phase (addition of particles) on the carrier phase as summarized by Madani et al. [43], i.e., data on the liquid phase only. In the following, research related to the measurements of both phases is outlined. A first PIV use in this context was performed by Virdung and Rasmuson [44] who used glass beads 1 mm in diameter that matched the refractive index of Benzyl alcohol/Ethanol mixture up to 1.5 v% volume fractions, suspended by the means of a pitched-blade impeller with a corresponding Reynolds number of Re = 7500. They showed that the r.m.s. velocities for both phases increased, whereas the velocity fields decreased overall with increasing particle concentrations. In addition, analysis of the mean axial slip velocity showed that particles lead the continuous phase in the impeller jet area and lag behind in the vertical stream close to the wall. Another study by Unakdat et al. [45] also used glass sphere particles of a size of 1 mm, suspended in water and thus without matching the liquid refractive index, reaching a dilute volumetric fraction of 0.5 v% operating at Re = 30,800. Consequently, the two phases were then separated by a phase discrimination technique based on the geometrical characteristics of the particles [46]. Results showed that particle turbulence levels measured at 0.5% were lower than the corresponding continuous phase without reports on the slip velocity. Further, Montante et al. [40] investigated the dilute suspension of 0.2 v% glass particles of sizes 115 and 774 µm in diameter without RIM (refractive index matching) of the liquid phase, at Re = 88,000 corresponding to a fully turbulent system. Phase separation was based on optical filters mounted on the cameras. Continuous-phase turbulence was found to reduce the values of particle settling velocity for the bigger particles, which was also reinforced by the approximate analysis of the force balance equation of the particles. A recent experimental study on this manner was communicated by Sommer et al. [47] that dealt with glass and polyethylene particles with a diameter range of 63–450 and various solid volume fractions. The camera used for the dispersed particle phase was based on shadowgraphy approach. The axial velocity of the glass beads, that possessed the highest inertia, was lower than the liquid mean flow velocity above and below the impeller. Comparisons also revealed that the axial turbulent fluctuations in the solid phase were lower than in the liquid phase, and this could be attributed to the huge difference between the depth of field (DOF) of the shadowgraphy camera (solid) and that of the PIV (liquid). The authors did not disclose any slip velocity analysis.

It is important to mention that Laser Doppler Velocimetry LDV is also a laser-based option for simultaneous data collection on solid and liquid flows in stirred tanks. Nouri and Whitelaw [48] used Diakon particles up to 2.5 v% concentration with size ranging from 590 to 730 µm to match the refractive index of Tetraline and Turpentine oil mixture and glass particles with water at dilute concentrations. The experiments were applied to different geometric set-ups and Re numbers. As a result, turbulence levels in the impeller stream were lower than the single-phase values (13–15%), with heavier particles exhibiting lower turbulence levels compared to lighter ones. Additionally, as particle concentration increased, the axial and radial particle mean velocities dropped by up to 5% in the impeller stream and 10% in the bulk of the flow. Since the measurement of liquid phase velocities in the presence of particles was not possible, the apparent relative velocity—which is the difference between particle velocity and that of the single phase—was discussed. They found that the apparent relative velocities of the glass particles were larger than those of the Diakon particles by factors of 2 and 2.5 in the impeller stream and in the bulk region, respectively. Guiraud et al. [49] analyzed the suspension of glass particles in water at low volume fraction 0.5 v% and diameter of 253 µm inside a stirred tank. Consequently, the r.m.s. axial particle velocities were always greater than those measured for the continuous phase, and the slip velocities were of the same order of magnitude as the terminal velocity evaluated by classical correlations.

As a reminder, the stirred tank in this work—dedicated for the mesenchymal stem cell MSC culture—has already been used to investigate practical aspects such as spatial distribution of microcarriers, just-suspended impeller speed, and the effect of particle loading on liquid-phase hydrodynamics [43]. Here, the simultaneous data acquisition of the solid–liquid flow of both phases inside the tank was obtained. That means that the system consists of microparticles whose density is very close to that of the liquid phase $\rho_p/\rho_f \approx 0.96$, a low-viscosity liquid, intermediate Reynolds numbers $Re \approx 5000$ and a low Stokes number $(St - 0.078 < 1)$. By the means of two-camera PIV, suspension of an RIM solid–liquid system was characterized to evaluate the velocities of the particles and the liquid phase, simultaneously, at various volume fractions ($0.1 < \alpha_p < 0.5$ v%). The interactions between both phases in terms of turbulence, slip velocities, and eventually interfacial forces were thus analyzed and discussed.

2. Materials and Methods

2.1. Experimental Set-Up

The investigated solid–liquid flow properties are exactly the same as those used to characterize the fluid phase previously [43], i.e., the effect of particle addition on the liquid phase up to $\alpha_p = 3$ v%. It is composed of PMMA microparticles (Cospheric) of d_p = 168 µm and ρ_p = 1185 kg/m^3 and Ammonium Thiocyanate NH_4SCN solution of 61 wt% corresponding to ρ_l = 1139.2 ± 0.1 kg/m^3 and μ_l = 1.94 ± 0.01 mPa.s. The solution was carefully filtered to remove any insoluble impurities (solid residues). Both phases were matched for a refractive index $RI \approx 1.491$. The volume fraction of the particles was systematically increased until it reached $\alpha_p = 0.5$ v% where significant noise made it impractical to treat images afterward despite the matching indices of both phases. The noise is evidently related to the images of particles in this case and not to the liquid phase. The maximum number of particles would thus be limited, around 1.4 million inside the tank.

As for the stirred tank (see Figure 1), it is made of borosilicate glass with a cylindrical body and hemispherical bottom shape, a diameter $T = 0.12$ m and a height of $H = 0.082$ m ($H/T = 0.68$). The impeller used is a three-blade axial-down-pumping mode HTPGD (Pierre Guerin [50]) with diameter D positioned at an off-bottom clearance C being $C/T = D/T = 0.5$. The tank is unbaffled but equipped with four dip tubes resembling the necessary sensors (temperature, pH, etc.), which play the same role as baffles and prevent the swirling phenomenon (See also Supplementary Materials). The working volume of the fluid phase is $V = 0.7L$ agitated at $N = 150$ rpm which corresponds to a full homogeneous suspension of PMMA microparticles. It is higher than the just-suspended state for all concentrations used as established by Delafosse et al. [51] on a solid–liquid system with the same properties. The resulting Reynolds number is around $Re \approx 5000$, indicating a relatively turbulent regime.

In addition, the stirred tank was held in an aquarium filled with paraffin oil of RI ≈ 1.468 (Fauth) to match the wall of the tank refractive index and thus limit the diffraction in the laser sheet due to the curvature of the body and the bottom side. The temperature was controlled by the means of an air conditioner inside the operating room (22–23 °C).

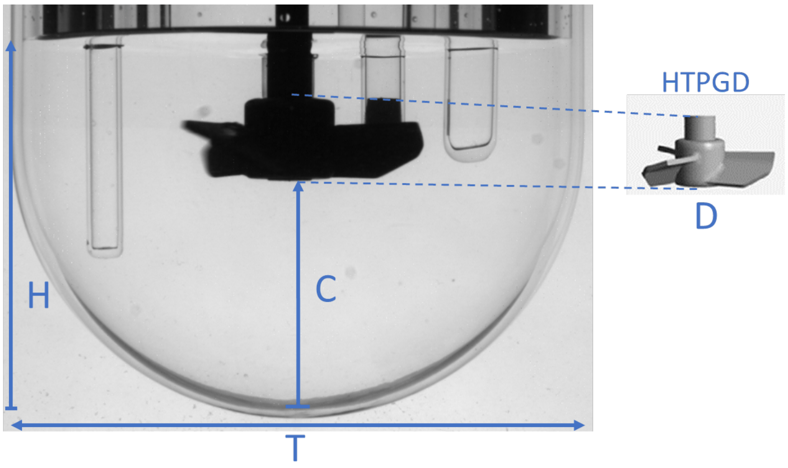

Figure 1. Geometrical configuration of the tank used equipped with HTPG down-pumping axial impeller. T = 0.12 m, H = 0.082 m. C/T = D/T = 0.5.

2.2. Simultaneous Two-Camera PIV

PIV technique was applied to simultaneously capture the continuous/carrier- and dispersed-phase flow fields in the vertical z-r plane at the center of the tank (measurement plane as seen in the green area in Figure 2 Left). The field of view captured thus corresponds to 80 × 60 mm which is half of the tank in the z-r plane. The system represented in Figure 2 was equipped with two CMOS cameras (FlowSense EO 4M), each with a 16 Hz maximum acquisition frequency and a 2048 × 2048 pixel resolution. To capture flow images separately, the cameras were mounted with wavelength-based optical filters. The illumination was provided by Nd:YAG double pulse laser of 532 nm wavelength operating at 50 mJ. A prism was located between the two cameras at 45° that allowed a straight vision of the tank for the "liquid" camera and acted as a mirror for the "solids" camera.

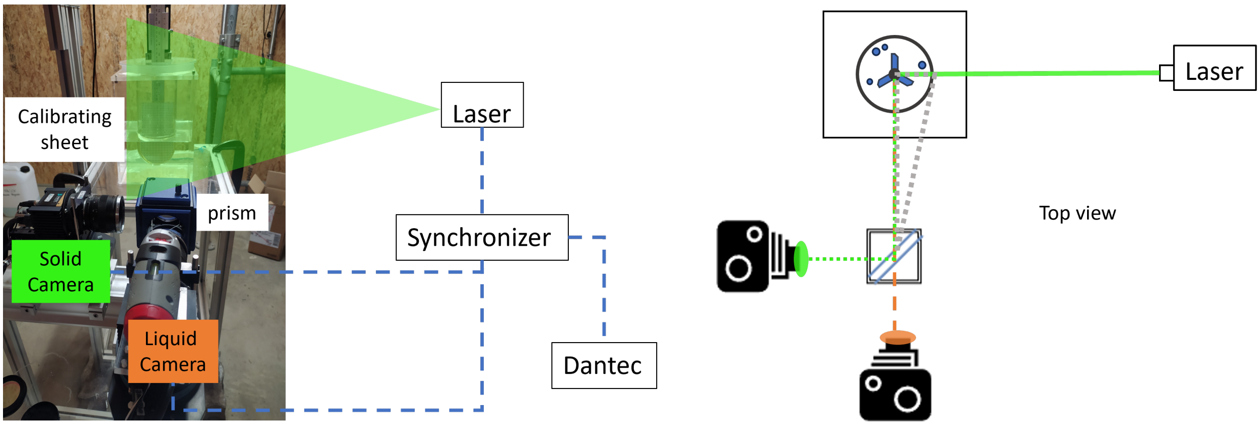

Figure 2. (**Left**): Simultaneous PIV set-up associated with a calibration sheet. (**Right**): Top view of the PIV set-up with the stirred tank. Liquid camera is equipped with an orange filter (>570 nm). Solids camera is equipped with a green filter (=530 nm). Laser sheet illuminates the center of the tank right at the shaft. The gray-dotted lines indicate the measurement plane perceived by the imaging system.

The two-phase flow was seeded with 20 µL Rhodamine-coated-PMMA fluorescent tracers (0.25 g/mL initial concentration, Dantec Dynamics v7.3), neutrally buoyant, with emission wavelength $\approx$ 590 nm, tracer diameter size of $d \approx$ 10 µm and density of ρ = 1190 kg/m^3. That being said, phase separation for images relied on the optical filters as mentioned above: the camera for the continuous liquid phase was fitted with a 570 nm orange filter that cuts off emissions below this wavelength, whereas the camera for the dispersed solid phase was equipped with a 530 nm green filter that reflects the laser sheet. Despite the RIM technique, PMMA microparticles are solely detected due to the presence of slight mismatches at the interface (between the dispersed phase and the liquid phase) that permit the high-intensity laser to be scattered by the particles. This point is heavily discussed in a previous study [43]. Moreover, the particles camera aperture was adjusted accordingly as a first step to minimize noise capture. The noise treatment is discussed in detail in the following section. With the time interval between two laser pulses fixed at Δt = 1500 µs—limiting tracer displacement in the impeller region to roughly one-quarter of the interrogation area—the two cameras, synchronized by an encoder, acquired images at the same instant. A set of 1100 image pairs was finally captured at an acquisition rate of 15.8 Hz and saved in the Dantec Dynamics software v7.3 for each case to ensure the statistical convergence of mean velocities and turbulent fluctuations.

2.3. Noise and PIV Treatments

When dealing with two-phase flows, optical separation is not enough for analysis. Noise treatment is crucial and essential prior to the application of cross-correlations to obtain vector maps. A step that is sometimes ignored or not shown in the research could support the reliability of the PIV raw images. First, the efficiency of optical filters was assessed by comparing images taken with the solid camera with and without fluorescent tracers (Figure 3). As one may notice, the tracers did not interfere or appear in the solid camera, as the emission was at a higher wavelength. This is an important check to verify that the particles tracked during the increase in volume fractions are PMMA particles per se and not tracers. Furthermore, considerable impurities can be present in salt solutions (NH_4SCN in this case) and can further alter image clarity and ultimately bias dispersed phase velocities; therefore, filtering the solution is a paramount checkpoint.

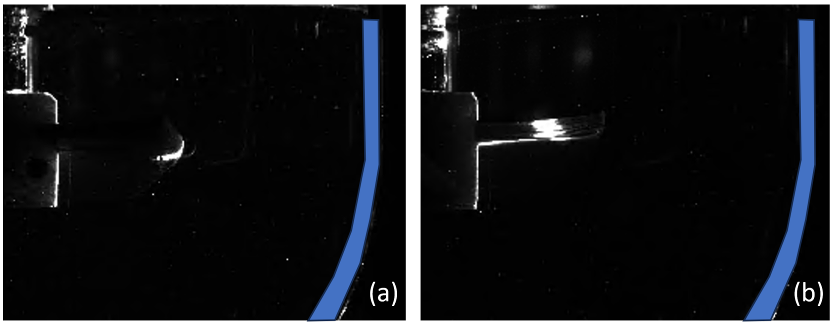

Figure 3. Solids camera snap-shot: (**a**) Without tracer particles. (**b**) With tracer particles.

Subsequently, the images registered for each camera were treated differently but with the same concept of creating a background image that represents noise and then subtracting the generated background from the raw images. The liquid-phase images followed the same approach as used before, by computing the minimum power mean grayscale values from the set of images (also known as a generalized mean) to form a unified background image. Insignificant noise was found at $\alpha_p = 0.5$ v%, as the presence of PMMA particles at these levels did not deteriorate the quality of the image, thanks to RIM between both phases. As previously mentioned, this was validated in a previous study [43]. On the other hand, for particle-phase images, a background needs to be created for every image. Since PMMA microparticles were added accordingly up to $\alpha_p = 0.5$ v%, noise propagated with increasing particle concentration, resulting in either high bright spots or gray areas in the images. An example is shown in Figure 4 where the generated background is subtracted from the raw image to eliminate as much noise as possible. The background creation was based on a sequence of image processing operations: a median filter, an erosion followed by a dilation, and finally a shock filter, each applied with a 5 × 5 pixel window (Dantec Dynamics v7.3). Noticeably, near the tank wall, where the laser first hits, low noise from PMMA microparticles is found, which is confirmed by the black area from the background image (Figure 4b) in that region. As the laser beam travels farther into the medium, PMMA-induced noise becomes increasingly prominent, but the four-stage image processing tool effectively removes this noise.

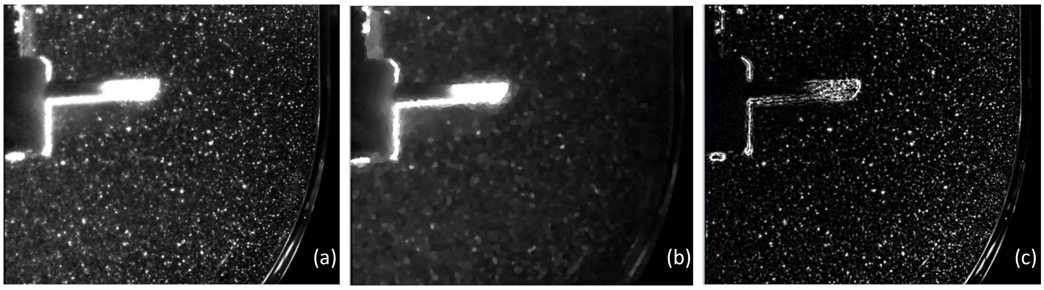

Figure 4. Instantaneous PIV images from solids camera at $\alpha_p = 0.5$ v%: (**a**) Raw image. (**b**) Generated background filter. (**c**) Treated image. The impeller is evidently masked prior to obtaining vector maps.

After the image treatment step, the instantaneous velocity maps were obtained for both phases using the open-source PIVLab toolbox (v3.02) [52,53]. Since the emergence of this tool, it has been extensively used and validated in various applications [54–57]. Multipass FFT window deformation scheme was used with a final window size of 32 × 32 pixel and 50% overlap, corresponding to a spatial resolution of $L_{IA} = 1.1$ mm. The ratio of spatial resolution to particle diameter is $L_{IA}/d_p = 6.5$, which means that it is large enough to acquire velocity vectors of PMMA particles that appear in the entire IA. Eventually, spurious vectors would emerge, and a validation step is necessary. For the liquid phase, the standard deviation (σ) of each vector map was computed; subsequently, any vectors that deviate from the mean by more than $3{\cdot}\sigma$ were disposed. With regard to dispersed phase, slightly more spurious vectors arose compared to the liquid phase, and the local median filter approach was thus utilized. Each velocity vector was compared with the median of the eight neighbours in a 3×3 window. This difference was then divided by the median of the eight differences inside the window to form a normalized residual k. Vectors that exceeded $3 \cdot k$ were then removed and considered invalid. More than 99% of the vectors passed the validation step for the liquid phase and around 97.5–98% for the particle phase, indicating a high-quality vector field. The results obtained were then post-processed in MATLAB (R2023b) for further analysis.

2.4. Flow Properties

One way to characterize turbulent levels inside the stirred tank is by estimating the turbulent kinetic energy TKE. It depends on the fluctuating velocity terms that could be evaluated using classical Reynolds decomposition $u' = u - \overline{U}$, where u is the instantaneous velocity and $\overline{U}$ is the time-averaged velocity, i.e., the ensemble-average of the 1100 set of the velocity fields. The mean velocity magnitude of the flow is defined as the square root of the sum of the squared velocity terms $M = \sqrt{\overline{U_r}^2 + \overline{U_z}^2}$. The subscripts r and z denote the radial and axial terms, respectively, with positive r directed to the right and positive z directed upward. The origin of the axis is located at the center of the tank bottom.

Note that the fluctuations contain periodic ones produced by the impeller, which can be isolated using an angle-resolved measurement. This study did not attempt to produce such information, which could be tackled in future work. In addition, Escudié and Liné [58] showed that the dissipation rates of mean and periodic kinetic energy were negligible compared to the dissipation rate of turbulent kinetic energy, so the use of classical decomposition is sufficient when angle-resolved technique is unavailable. Theoretically, TKE is half of the trace of the Reynolds stress tensor, which means knowledge of the three terms of the fluctuating velocity components (radial, axial and tangential), whereas the experimental set-up employed here is a 2D PIV system. In this case, where the tangential component is unknown, a pseudo-isotropic scheme may be applied [45,59,60] so that TKE $k = \frac{3}{4}\left(\overline{u_r'^2} + \overline{u_z'^2}\right) = \frac{3}{4}\left(\overline{Urms_r}^2 + \overline{Urms_z}^2\right)$. The root mean square r.m.s. velocity $\overline{Urms} = \sqrt{\overline{u'^2}}$ also gives a single representative magnitude of these fluctuations. Additional comments on the Kolmogorov scale and the Taylor microscale could be found in [43].

Lastly, the velocity and turbulent kinetic energy terms are non-dimensionalized by (ND) and $(ND)^2$, respectively. The non-dimensional terms are denoted by a '*' as in $M^* = M/(ND)$ and $k^* = k/(ND)^2$ for instance. Note that this scaling is different from normalizing by the maximum tangential blade-tip velocity, $V_{tip} = \pi ND$, which introduces a factor of π.

Acquiring data at the same instant with unified spatial resolution opens the door for further analysis of the flow, specifically the particle–fluid slip velocity. It is the difference between the velocity of the particle phase and that of the liquid phase on either axis, that is, the velocity of the particle relative to the local fluid velocity, associated with a directional term, $u_s = (u_p - u_l)\ \frac{u_p}{|u_p|}$. The directional vector is added to govern the sign of the momentum transfer between phases [44]. Slip velocities are negative for areas where the continuous phase leads the dispersed phase and vice versa. The subscripts p and l are denoted for particles and liquid, respectively; e.g., $u_{p,z}$ is the instantaneous axial velocity for the particles. Using the terminal velocity experiments of PMMA particles, established previously in a still liquid, the axial slip velocity can be normalized by the terminal velocity, u_s/u_t.

3. Results and Discussions

First, several instantaneous superimposed vector maps of both particles (red) and liquid phases (blue) are shown in Figure 5, where one may notice that the velocity vectors are not perfectly matched, yet not completely diverted. The main difference that could be spotted is not only the magnitude, but also the orientation of the vectors, i.e., the angle between the velocity vectors, especially in the impeller region. The extent of such variations will be further discussed in the slip velocity Section 3.2.

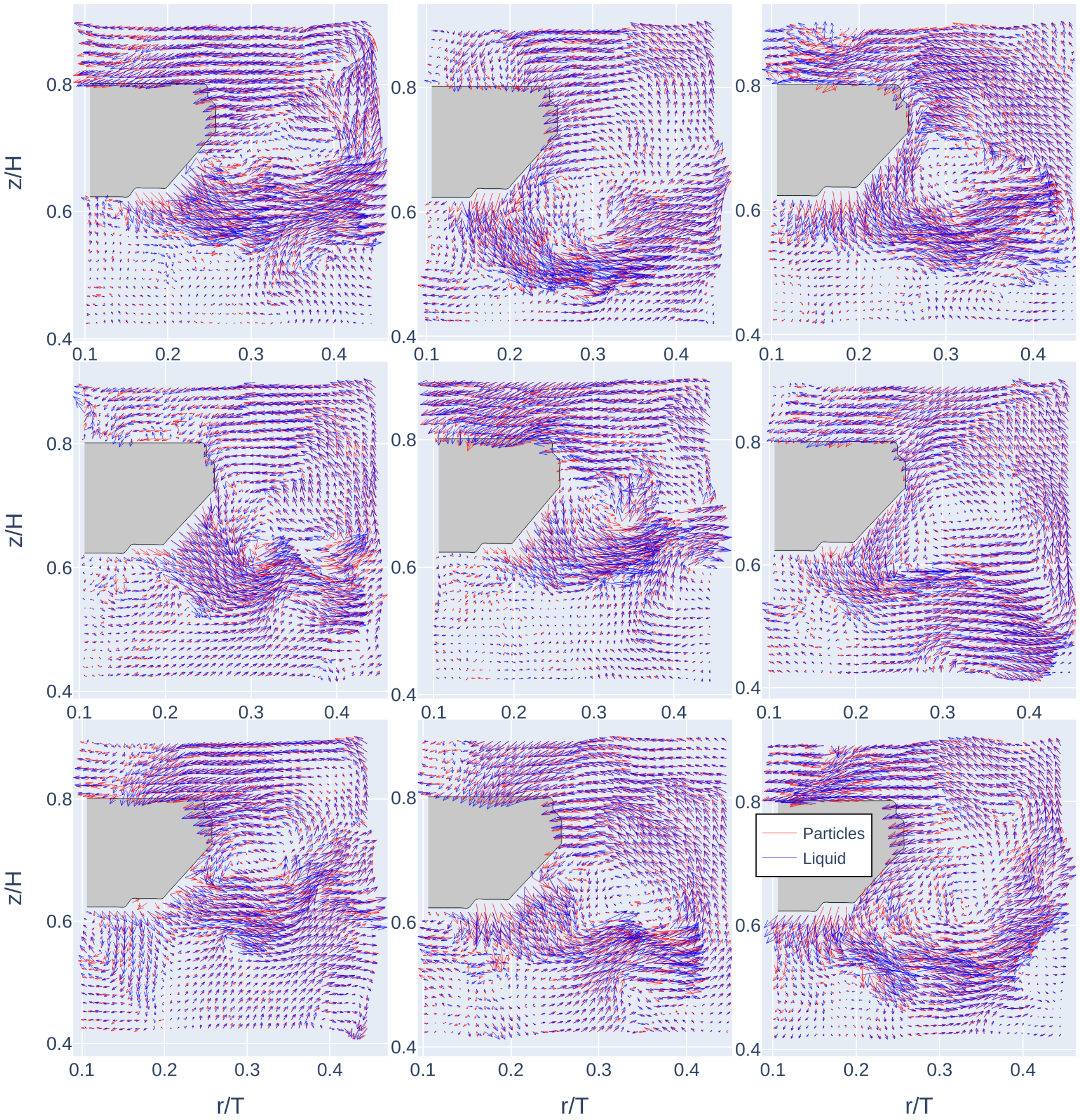

Figure 5. Case α_p = 0.5 v%: Superimposed instantaneous velocity vectors of particles (red) and liquid (blue) phases for different snap-shots. Geometry is limited here to the impeller region for a clear view of velocity vectors.

The scheme presented in Figure 6 is used as a reference in the following sections. It shows the axial/vertical profiles at r/T = 0.22 and 0.48, as well as an area of 10 × 10 mm, located at 0.57 < z/H < 0.67 and 0.22 < r/T < 0.32, in the impeller discharge region. The first vertical profile at r/T = 0.22 passes through the impeller to cover the discharge flow and the ending phase of the recirculation loop. The second vertical profile at r/T = 0.48, near the wall, covers the other half of the loop where the up-flow part takes place and where low-to-moderate values of the properties investigated (e.g., velocity, turbulence) are observed. These profiles and values locally averaged on the square area will be used for the analysis in the upcoming sections.

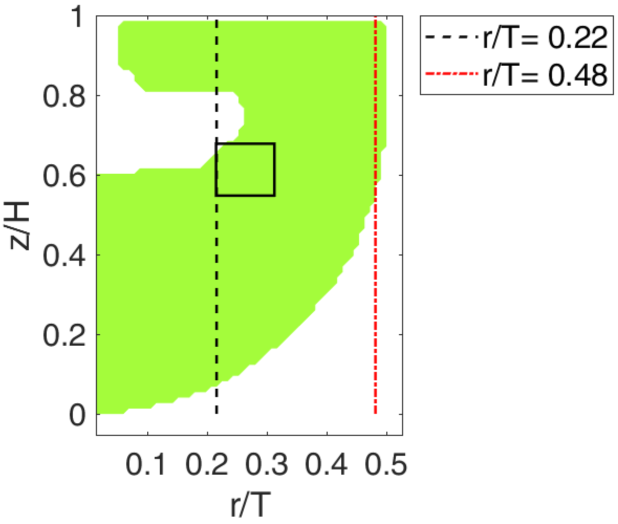

Figure 6. Scheme showing relative cross sections/profile cuts and local area (box) positions for further analysis. The area/box is located at 0.57 < z/H < 0.67 and 0.22 < r/T < 0.32.

3.1. Flow and Turbulence Analysis

Contour plots in Figure 7 show that the liquid mean velocity is essentially unchanged from α_p = 0 to 0.5 v% (panels a–b, respectively), whereas the solid phase mean velocity at α_p = 0.5 v% (panel c) is reduced in the impeller discharge region. Both the fluid velocity contours (with and without particles) and the particle velocity contours exhibit the same down-pumping axial flow in the measured plane. The resulting circulating loop starts at the lower side of the impeller tip and extends toward the wall where the flow changes its direction upward to finally close the loop at the upper side of the impeller tip. It is apparent that the values of the mean velocity at the end of the loop above the impeller tip are consistently higher than those near the wall. This difference arises from the impeller pushing the flow, which entrains fluid and particles from the upper region as it sweeps through the volume. The center of the loop is located between 0.3 < r/T < 0.4 and 0.65 < z/H < 0.75. Under the impeller, there is a region of almost stagnant flow in the measurement plane, where the unmeasured off-plane tangential flow is predominant. The maximum velocity magnitude in the impeller discharge is around $1.1ND = 0.35V_{tip}$ for both liquid phases. On the other hand, the contour plot of the mean velocity of the solid phase at α_p = 0.5 v% possesses lower values in the impeller stream (Figure 7c) around $0.85ND = 0.27V_{tip}$ compared to the former contours. Note that the mean velocity vectors (white) of each corresponding case are also plotted in the contour images.

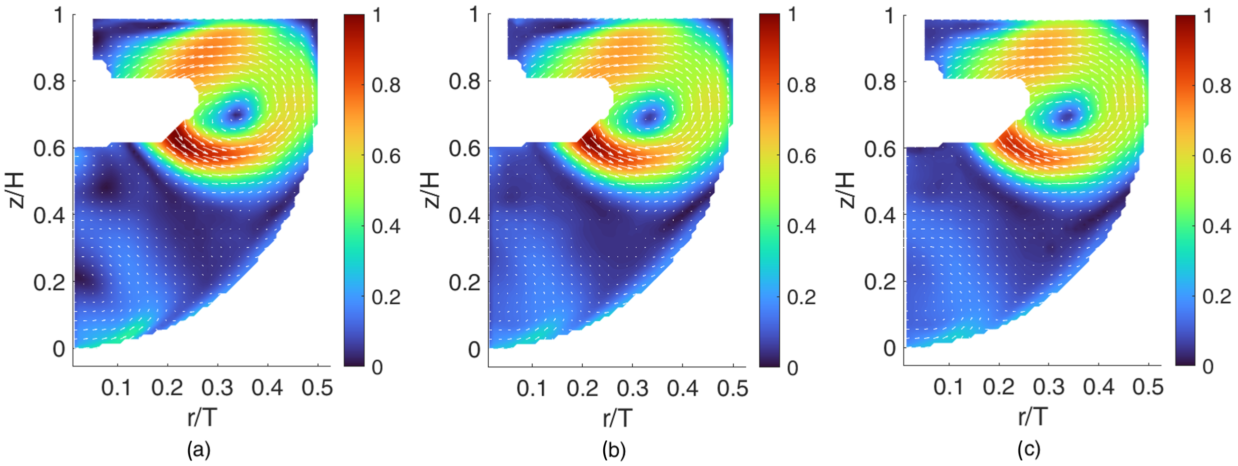

Figure 7. Non-dimensional mean velocity magnitude of the flow M^*, scaled by (ND): (**a**) Single-phase flow, (**b**) liquid phase for α_p = 0.5 v%, (**c**) solid phase for α_p = 0.5 v%. The corresponding mean velocity vectors are added to each contour plot. Color-bar: $M^* = M/(ND)$.

For a more detailed, quantitative comparison, the velocity profiles are shown in Figures 8 and 9, arranged according to the scheme presented previously in Figure 6. The evaluation is between single phase (without particles) on one hand, and liquid phase and solid phase at the maximum solid concentration reached α_p = 0.5 v% on the other hand. Figure 8 shows the mean radial (Figure 8 Left) and axial (Figure 8 Center) velocities, $\overline{U}_r^*$ and $\overline{U}_z^*$, respectively, as well as the velocity magnitude (Figure 8 Right) M^* along the vertical profile at r/T = 0.22. As mentioned above, this profile passes through the impeller jet stream. For the mean radial velocity, negligible variations are found for the liquid phase with α_p = 0.5 v% and without particles. The solid phase at α_p = 0.5 v% also exhibits the same behavior except for the impeller discharge at 0.6 < z/H < 0.65, where mean radial values drop by 12%. Moving to the mean axial velocity, at 0.6 < z/H < 0.65, single phase carries higher mean axial values than that of liquid phase at α_p = 0.5 v% with a drop of 13%, whereas the particles' mean axial velocity at the same concentration hold even lower values in the same region, with 11% decrease from that of the liquid phase and a maximum of 20% decrease from that of the single phase. Otherwise, the three examined cases are almost identical elsewhere in the profile plot. The combination of radial and axial terms into mean velocity magnitude further demonstrates the differences observed between solid and liquid phases in the same region 0.6 < z/H < 0.65, with a maximum damping of 18%. Aside from the impeller region, the local velocity magnitudes remain essentially unchanged by the addition of particles.

Near the wall, at r/T= 0.48, where lower velocities are present, small differences can be noticed on Figure 9. For the mean radial velocity term $\overline{U}_r^*$ (Figure 9 Left), liquid phase at α_p = 0.5 v% is slightly greater than that of single phase and dispersed phase by ≈ 12% along the z-axis at 0.6 < z/H < 0.65 and 0.8 < z/H < 0.9. However, for the mean axial velocity term (Figure 9 Center) and velocity magnitude (Figure 9 Right), particles lead the liquid phase without and with α_p = 0.5 v% fractions along the z-axis by ≈ 10%. Although the variations at r/T = 0.48 are considered not as significant as those at r/T = 0.22, one may notice that the behavior near the wall is opposite to that in the impeller region, where the particles lead in the zone near the wall and lagged behind in the impeller vicinity. Note that a radial plot is reported in Appendix A in Figure A1.

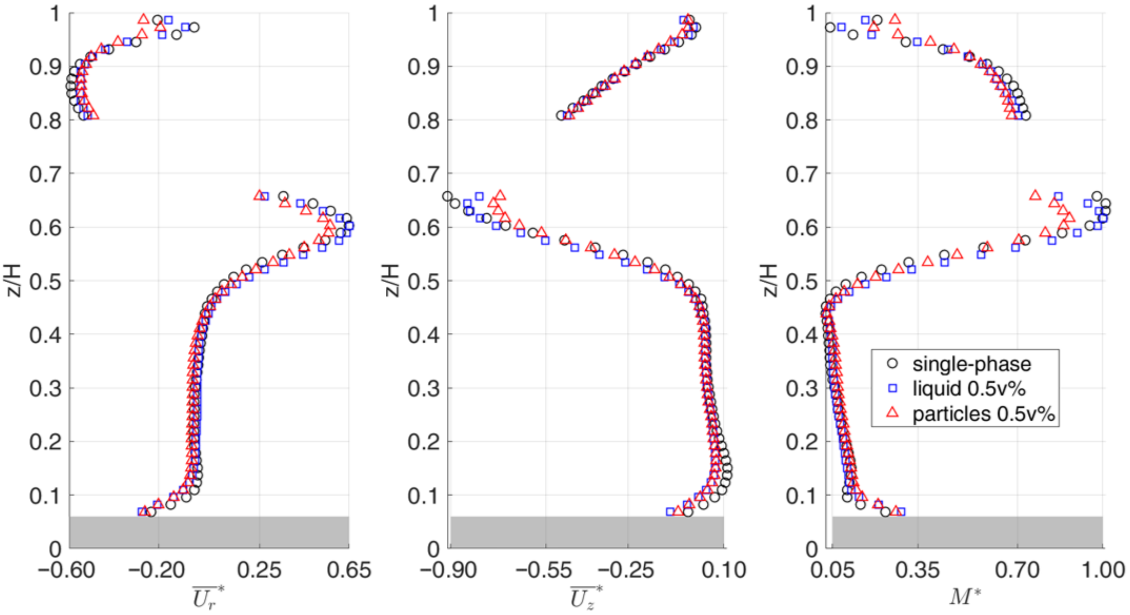

Figure 8. Non-dimensional mean velocity profile plots at r/T = 0.22, scaled by (ND): (**Left**) Mean radial velocity $\overline{U}_r^*$. (**Center**) Mean axial velocity $\overline{U}_z^*$. (**Right**) Mean velocity magnitude M^*. ◯: Single phase, □: Liquid phase at α_p = 0.5 v%, △: Solid phase at α_p = 0.5 v%. Gray-shaded area corresponds to tank edge; outside the measurement plane.

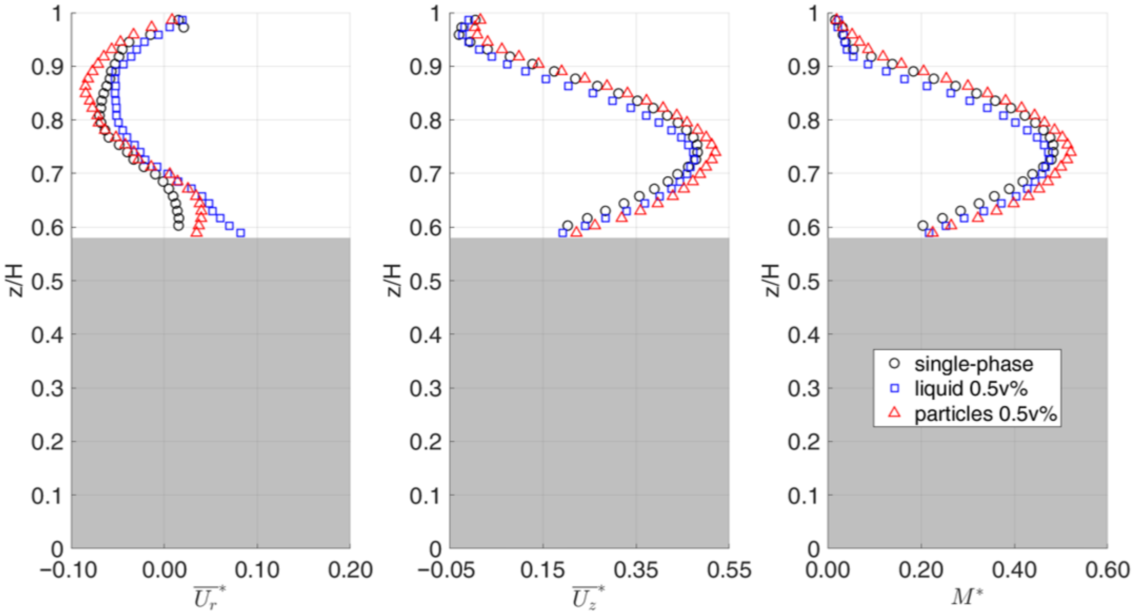

Figure 9. Non-dimensional mean velocity profile plot at r/T = 0.48, scaled by (ND): (**Left**) Mean radial velocity $\overline{U}_r^*$. (**Center**) Mean axial velocity $\overline{U}_z^*$. (**Right**) Mean velocity magnitude M^*. ◯: Single phase, □: Liquid phase at α_p = 0.5 v%, △: Solid phase at α_p = 0.5 v%. Gray-shaded area edge; outside the measurement plane.

Moving on to the turbulence levels, more clear and obvious differences are spotted in the contour plots of Figure 10. The figure shows the mean turbulent kinetic energy TKE k^* of the single-phase flow (Figure 10a), liquid phase at α_p = 0.5 v% (Figure 10b) and solid phase (Figure 10c) at the same particle volume fraction. The TKE attains its maximum value in the flow discharge region and progressively decreases toward the wall, as expected. This covers the bottom-half of the flow circulating loop. In the last phase of the circulating loop, above the impeller, low quantities of turbulence are also depicted. When comparing the liquid phases with and without particles, the TKE just at the blade tip is consistent with a maximum value reaching $k_l^* = 0.3(ND)^2 \approx 0.03V_{tip}^2$, while in the area around it, liquid-phase turbulence with α_p = 0.5 v% has slightly higher magnitudes. As for the solid-phase turbulence at α_p = 0.5 v%, the behavior is clearly different, where TKE is much lower in the impeller vicinity compared to both liquid cases, averaging around $k_p^* = 0.2(ND)^2 \approx 0.02V_{tip}^2$, that is, 1.5 times lower than the corresponding liquid-phase peak, highlighting a visible damping effect of particle addition on solid-phase turbulence.

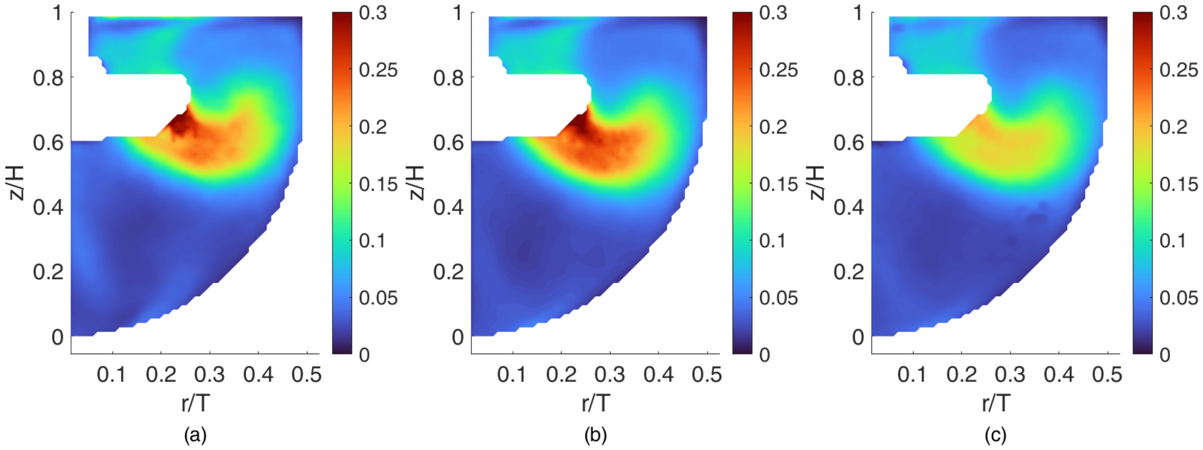

Figure 10. Non-dimensional mean turbulent kinetic energy TKE k^*, scaled by $(ND)^2$: (**a**) Single-phase flow, (**b**) liquid phase for α_p = 0.5 v%, (**c**) solid phase for α_p = 0.5 v%. Color-bar: $k^* = k/(ND)^2$.

In order to further analyze the observed phenomenon in the contour plots, the same approach as the flow velocity is used to compare the profile cuts at the positions mentioned previously in the scheme of Figure 6. These profiles are depicted in Figure 11 and Figure 12 at r/T = 0.22 and r/T = 0.48, respectively. Recall that at r/T = 0.22 is the axial cut that passes through the impeller region; Figure 11 shows the root mean square r.m.s. velocities of the radial (Figure 11 Left) and axial (Figure 11 Center) terms, $\overline{Urms}_r^*$ and $\overline{Urms}_z^*$, respectively, as well as the turbulent kinetic energy TKE (Figure 11 Right) k^*. Generally, the liquid-phase turbulence levels slightly edge over the single phase and solid phase at 0.5 < z/H < 0.65 in all examined terms. For the radial term), differences reach 12%, whereas for the axial term, liquid phase with and without particles plots are relatively coincided, and the recorded differences are around 15% higher than the solid phase. Eventually, the drop in turbulence levels between liquid phase and solid phase at α_p = 0.5 v% increases up to 30% for TKE plot in the same region 0.5 < z/H < 0.65. A minor damp is also observed for the single phase by around 10% at that position; this was observed in the contour plot of Figure 10 and previously established by another work [43].

On the wall side, where low levels of turbulence appear, a profile cut at r/T = 0.48 is covered in Figure 12. The radial r.m.s. velocity plot $\overline{Urms}_r^*$ (Figure 12 Left) highlights that the solid phase values at α_p = 0.5 v% surpass those of the single phase and liquid phase at the same concentration by 28%. This effect is drastically diminished for the axial term $\overline{Urms}_z^*$ (Figure 12 Center), where the three plots are almost overlapping. At last, the resulting TKE (Figure 12 Right) k^* reveals a 15% increase for the solid phase near the wall; however, the values at that position are very low, and, thus, the difference could be considered insignificant.

To examine the extent of the change in turbulence levels in the impeller region, a local average area is outlined. The idea is to spatially average the TKE in that region of interest, instead of showing several profile plots. This allows us to trace any possible effect over the particle volume fractions examined. The position of this area/box is depicted in Figure 6. The results shown in Figure 13 are the locally averaged TKE k^* values as a function of particle loading α_p for both carrier and dispersed phases. As previously reported, a 10% increase in turbulence is noticed for the liquid phase, from particle-free to α_p = 0.5 v%. This slight augmentation starts at α_p = 0.4 v%, while it is the same levels of turbulence for other cases. Conversely, TKE values decline substantially between α_p = 0.1 v% and 0.5 v% by 25% in the impeller region. Upon comparing both phases, it is noticeable that at α_p = 0.1 v%, particle turbulence is marginally higher than that of the liquid part, within the experimental deviations. Increasing the volume fractions to α_p = 0.2–0.3 v% diminishes any variations, while from α_p = 0.4–0.5 v%, the liquid phase possesses higher values, as seen previously, with differences being 12% and 30%, respectively, in that region.

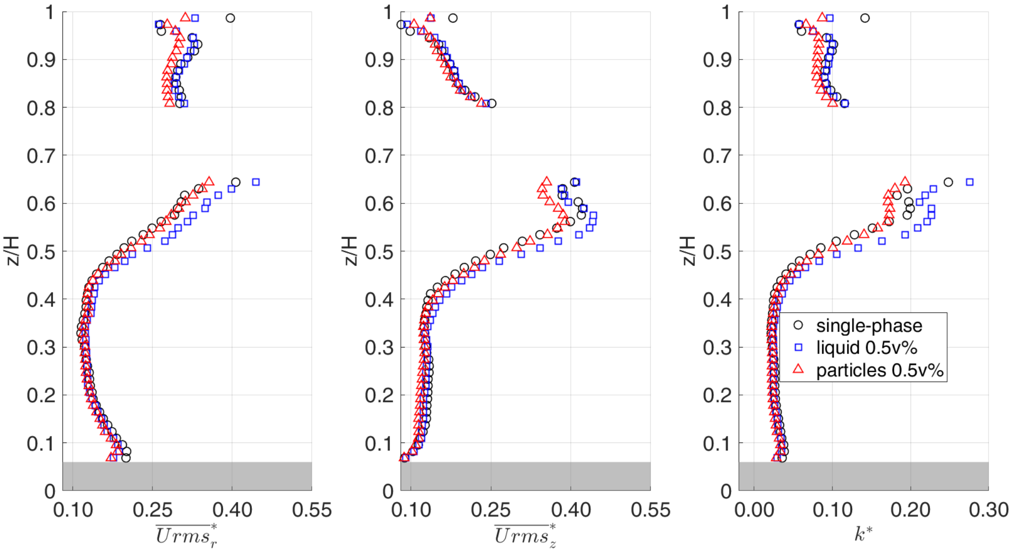

Figure 11. Non-dimensional turbulence terms profile plots at r/T = 0.22, scaled by $(ND)^2$: (**Left**) Mean radial r.m.s. velocity $\overline{Urms}_r^*$. (**Center**) Mean axial r.m.s. velocity $\overline{Urms}_z^*$. (**Right**) Turbulent kinetic energy TKE k^*. ◯: Single phase, □: Liquid phase at α_p = 0.5 v%, △: Solid phase at α_p = 0.5 v%. Gray-shaded area corresponds to tank edge; outside the measurement plane.

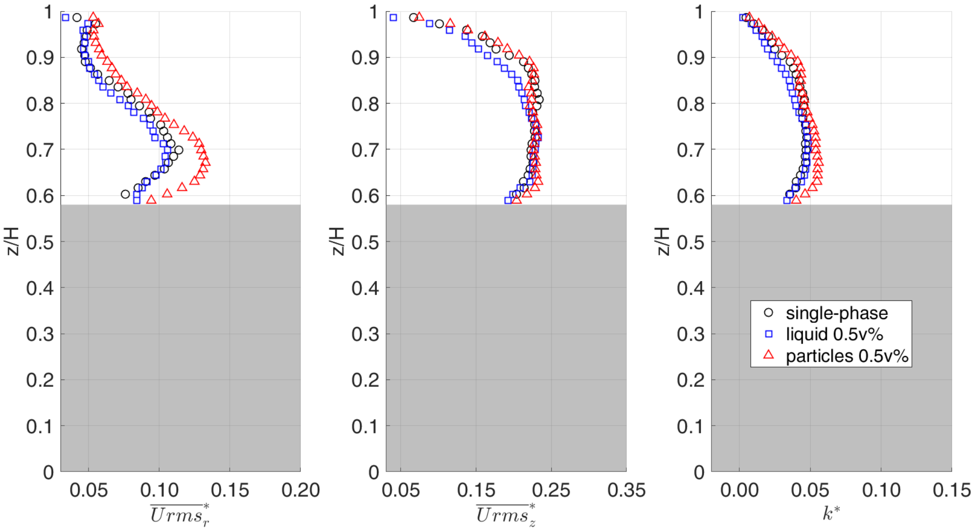

Figure 12. Non-dimensional turbulence terms profile plot at r/T = 0.48, scaled by $(ND)^2$: (**Left**) Mean radial r.m.s. velocity $\overline{Urms}_r^*$. (**Center**) Mean axial r.m.s. velocity $\overline{Urms}_z^*$. (**Right**) Turbulent kinetic energy TKE k^*. ◯: Single phase, □: Liquid phase at α_p = 0.5 v%, △: Solid phase at α_p = 0.5 v%. Gray-shaded area corresponds to tank edge; outside the measurement plane.

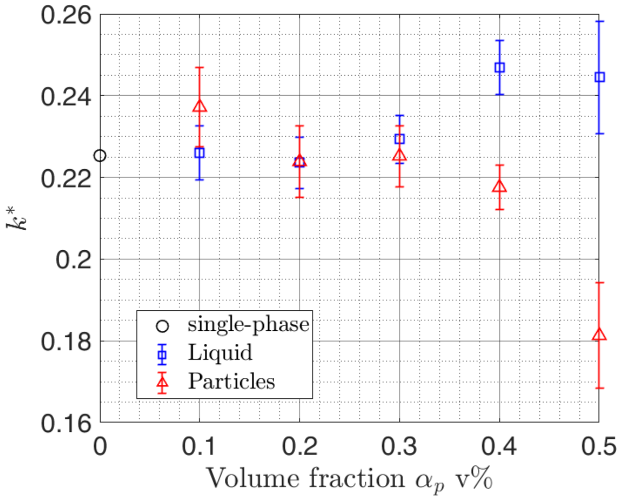

Figure 13. Local average of non-dimensional turbulent kinetic energy TKE k^* scaled by $(ND)^2$; it is averaged in the area/box depicted in Figure 6 in the impeller region, as a function of different volume fractions α_p v%. ○: Single phase, □: Liquid phase, △: Solid phase.

Interestingly, one can replot a comparative axial profile cut at r/T = 0.22 between the standout cases. Figure 14 reveals the ratio of TKE of the solid phase to that of the liquid phase k_p^*/k_l^* for α_p = 0.1, 0.4 and 0.5 v%. For reference, a solid vertical line is also shown as a unity. For α_p = 0.1 v%, the ratio k_p^*/k_l^* is generally higher than 1, and it could reach 1.2–1.4 times in the impeller stream, only to drop to 0.95 at 0.4 < z/H < 0.6. However, at α_p = 0.4 and 0.5 v%, the ratio k_p^*/k_l^* is always lower than 1, varying around 0.85. At 0.4 < z/H < 0.6, the TKE ratio drops even lower for α_p = 0.5 v% to reach 0.5. This means that TKE of the dispersed phase drops 50% compared to that of the liquid phase in this segment. Few researchers revealed the same response of particles in terms of turbulence levels. Unakdat et al. [45] noticed a drop in r.m.s. intensities with increasing volume fractions (at α_p = 0.5 v%). Sommer et al. [47] also reported a drop in the turbulence levels of the solid phase, with values always lower than that of the liquid phase (at α_p = 0.1 v%), whereas Virdung and Rasmuson [44] observed an opposite pattern, where turbulence levels for both solid and liquid phases increased with the addition of particles (at α_p = 1.5 v%).

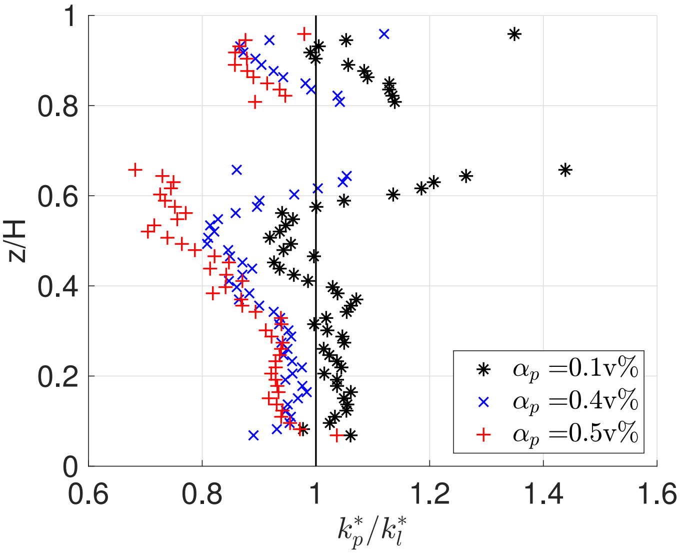

Figure 14. Ratio of particle-to-liquid turbulent kinetic energy TKE k_p^*/k_l^* profile plot at r/T = 0.22. ∗: α_p = 0.1 v%, ×: α_p = 0.4 v%, +: α_p = 0.5 v%.

3.2. Slip Velocity

As discussed previously, the slip velocity quantifies the relative motion between the dispersed particles and the carrier fluid. In this section, we present the differences in slip velocity values, which could be further influenced by the vector orientation of each phase in the 2D vertical plane. In some areas, mainly in the impeller, wall, and bottom regions, few distinctions are noticed in terms of angle deviations between the velocity vectors of each phase, which can be referred to in Figures A2 and A3 (see Appendix A). In Figure 15, the slip velocity divided by the terminal velocity of particles in still liquid U_s/U_t is shown as a contour plot. The first row represents the case α_p = 0.1 v%, while the second corresponds to the case α_p = 0.5 v%. Column-wise, from left to right, the contours are listed as radial, axial, and magnitude, respectively. The effect of increasing the particle loading is then discussed for each term. Note that the value of U_t is estimated from independent settling experiments following Delafosse et al. [51]; the resulting value is around 6.5×10^{-4} m/s.

For the radial term, an interesting behavior is noticed in the impeller region, from α_p = 0.1 v% (Figure 15a) to α_p = 0.5 v% (Figure 15d). In Figure 15a, in the impeller region, specifically at 0.5 < z/H < 0.7 and 0.2 < r/T < 0.3, radial slip velocity is split into a positive sign reaching $10U_t$ in the upper area and a negative sign in the lower area around $-5U_t$. Recall that the biggest impact is near the center of the circulating loop, where lower velocities exist (Figure 7). Nevertheless, the particle leads radially in that region toward the wall and lags behind the liquid phase below that area. Regarding Figure 15d, the phenomenon is almost diminished; the positive sign region near the center of the loop drops to $1.5U_t$, whereas in the region corresponding to the flow stream, the radial slip velocity increases to $-10U_t$. It is worth mentioning that near the surface, at z/H ≈ 1, high radial slip velocities are found, which could be attributed to some experimental deviations there. Globally, for both cases, the radial slip velocity varies between $-U_t$ and U_t.

Concerning axial slip velocities for α_p = 0.1 v% and 0.5 v%, the corresponding contour plots are shown in Figure 15b and Figure 15e, respectively. Visually, the effect of rising particles concentration is clearer in the impeller stream zone. An increase in axial slip velocity is observed up to $-10U_t$, as well as an increase in the area. That is, the axial slip also increased with increasing particle concentration. Markedly, the negative sign means that particles are slower in the impeller flow stream than the carrier fluid. In contrast, near the wall where upward flow takes place, particles deviate faster from the wall to the domain than the fluid, especially with α_p = 0.5 v%. A further discussion on this matter follows shortly thereafter. Overall, similar to the case of the radial term, the axial slip velocities shift between $-U_t$ and U_t.

In Figure 15c and Figure 15f, the slip velocity magnitude is displayed, which combines both axial and radial slip terms, for α_p = 0.1 v% and 0.5 v%, respectively. An increase in the mean slip velocity is noticed with the increase in particle volume fractions, specifically in the impeller and wall zones. This is in agreement with Sardeshpande et al. [61] who demonstrated the same trend of slip velocity data as a function of particle concentration.

Arguably, some studies detected an inverse behavior to the one reported by our study, where particles lead the fluid phase in the downward-accelerating flow and lag behind in the upward stage, such as Nouri and Whitelaw [48], Virdung and Rasmuson [44], and Montante et al. [40] in their experimental point of view, as well as Ljungqvist and Rasmuson [62] who mentioned that the computational model always predicts that the particles move downwards more rapidly and upwards more slowly than the fluid phase. The possible explanation for this could be due to the inertia of particles. However, in their experimental data, Ljungqvist and Rasmuson [63] also mentioned that the opposite situation occurs in some parts of the tank. Other authors who reported that the particles are slower in the downward flow and faster in the upward flow with respect to the fluid phase are Giraud et al. [64], Sardeshpande et al. [61], and Sommer et al. [47], who noticed that the particle axial velocity was lower than the liquid mean flow velocity above and below the impeller. Since the particles were not fully suspended in the system, the overall decrease in particle axial velocity could be attributed to the sedimentation of particles. It should be noted that for all the studies mentioned, the particle size used is on average 4–9 times greater than the PMMA microparticle size, and the density ratio between both phases is $\rho_p/\rho_l \gg 1$ much greater than $\rho_p/\rho_l \approx 1$ used in this study.

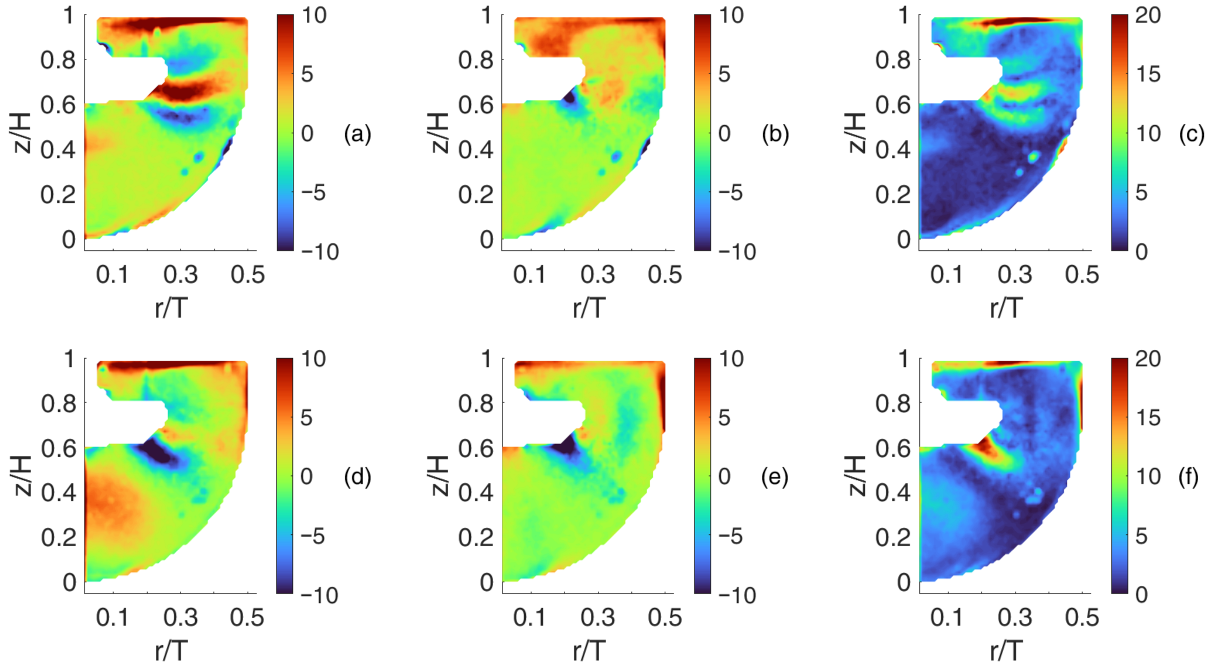

Figure 15. Non-dimensional mean slip velocity data scaled by terminal velocity U_s/U_t for α_p = 0.1 v% (1st row) and α_p = 0.5 v% (2nd row). Column-wise: 1st column: Mean radial slip velocity $U_{s,r}/U_t$ (**a**) α_p = 0.1 v%, (**d**) α_p = 0.5 v%. 2nd column: Mean axial slip velocity $U_{s,z}/U_t$ (**b**) α_p = 0.1 v%, (**e**) α_p = 0.5 v%. 3rd column: Mean slip velocity magnitude U_s/U_t (**c**) α_p = 0.1 v%, (**f**) α_p = 0.5 v%. Color-bar: U_s/U_t.

Accordingly, additional comparisons with correlations from the literature are invoked for a more valid analysis. One is the correlation previously demonstrated by Pinelli et al. [65] and a suggested modification by Fajner et al. [66] to include the effect of the density difference between the dispersed and carrier phases and some adjustments to the correcting terms

$$\frac{U_s}{U_t} = 0.6 + 0.32\,\tanh\!\left[19\,\frac{\eta}{d_p}\left(\frac{\rho_p-\rho_l}{\rho_l}\right)^{0.5} - 1\right] \tag{1}$$

where η is the Kolmogorov length scale, and U_s and U_t are the settling velocities in turbulent and quiescent fluids of the empirical model, respectively. Note that U_s in definition, is referred to as the slip velocity, which is essentially the effective settling velocity of the particle in a turbulent fluid. Another correlation proposed by Lane et al. [67] where the effect of turbulence on the drag coefficient was correlated in terms of Stokes number

$$\frac{U_s}{U_t} = 1 - 1.4\,St^{0.7}\exp(-0.6\,St) \tag{2}$$

The Stokes number St used in their model relates the particle relaxation time to the integral time scale of the carrier fluid and not to the Kolmogorov time scale. The key parameter between the two models is that Equation (1) depends on the length scale ratio (η/d_p) of the domain, whereas Equation (2) contains the time scale ratio (St), which permits more valid comparisons. Note that the required characteristic scales of the system, i.e., the Kolmogorov length scale and the integral time scale, were estimated from the mean power dissipation based on the impeller power number (Np = 0.67 [68]).

Aside from the impeller and wall regions where high differences appeared, both radial and axial slip velocities are in good agreement with the proposed correlations. The spatial average for the radial and axial slip velocities divided by the terminal velocity U_s/U_t of the experiments leads to 0.7 and 0.85, respectively, for both α_p = 0.1 v% and 0.5 v%. Even when the domain is averaged, including the high-slip-velocity zones, the total average increases to U_s/U_t = 0.9 and 1.1 for radial and axial terms, respectively. On the other hand, the correlations would predict 0.92 and 0.96 for Equation (1) and Equation (2), respectively. This suggests that U_s/U_t, on average, is less than unity. Taking into account exclusively the impeller zone, the slip velocity is higher than the values predicted by the literature, which could be attributed to the acceleration phase experienced by the particles.

Previous authors reported high slip velocities in the impeller region for different radial and axial flow geometries. In the experiments of Montante et al. [40], they noticed the same order of slip velocity in the high-accelerating-flow zone $U_s/U_t > 10$. Within the realm of CFD work and validation, Derksen [69] observed a dominance of high slip velocity in the impeller zone, and all drag models used were able to capture this behavior. Ljungqvist and Rasmuson [62] found that the enhanced drag model utilized [70], which accounts for free-stream turbulence, resulted in a severe underestimation of radial and tangential slip velocities and overestimation of the axial slip, whereas Sardeshpande et al. [61] indicated that drag correlation proposed by Brucato et al. [70] overpredicted experimental axial slip velocity near the impeller region. Consequently, it was more appropriate to use the measured local slip velocity to evaluate and modify different interphase drag correlations.

3.3. Contributing Forces

Furthermore, the slip velocity data obtained from the experiments are incorporated into the force balance equation (Equation (3)) of a single spherical particle, suspended in an unsteady and non-uniform flow field [71,72]. The tentative evaluation of the contributing forces was only approached experimentally by Montante et al. [40]. As the authors explained, various assumptions were made: the contribution of the tangential velocity component, wall interactions, shear rate forces, and the effect of the rotation of particles are not considered. Thus, the scalar force balance equation in the vertical direction z using the mean velocity data can be approximated as follows:

$$-\rho_p\,\overline{U}_{p,z}\,\frac{d\overline{U}_{p,z}}{dz}+\rho_l\,\overline{U}_{l,z}\,\frac{d\overline{U}_{l,z}}{dz}-F_M-F_L-F_D-(\rho_p-\rho_l)\,g=0 \tag{3}$$

$$\begin{cases} F_M=\rho_l\,C_M\left(\overline{U}_{p,z}\,\dfrac{d\overline{U}_{p,z}}{dz}-\overline{U}_{l,z}\,\dfrac{d\overline{U}_{l,z}}{dz}\right), \\ F_L=\rho_l\,C_L\,(\overline{U}_{p,r}-\overline{U}_{l,r})\left(\dfrac{d\overline{U}_{l,r}}{dz}-\dfrac{d\overline{U}_{l,z}}{dr}\right), \\ F_D=\dfrac{3}{4}\,\rho_l\,\dfrac{C_D}{d_p}\,(\overline{U}_{p,z}-\overline{U}_{l,z})\left|\overline{U}_{p,z}-\overline{U}_{l,z}\right| \end{cases}$$

From left to right, the contributing forces are particle inertia, liquid pressure gradient, virtual added mass, lift, drag, and finally the combination of gravity and buoyancy forces. The equation is divided by the unit volume of a single particle; thus, the unit of forces is

N/m^3. The coefficients C_M, C_L and C_D represent the added mass, lift, and drag, respectively. The particle lift coefficient is based on Saffman correlation only, since PIV cannot provide information on the rotation of particles, while particle drag coefficient is based on the Oseen model [73]. The various estimated terms of the force balance equation are approximate, yet valuable insights are obtained for a better understanding of the system.

Figure 16 shows the contributions of the different forces in the approximate scalar equation for the case α_p = 0.5 v%. The terms are listed as in (Equation (3)), starting with particle inertia, then fluid pressure gradient, added mass, and lift force. These terms are found in the first row of the figure as they share the same scale. In the second row, the drag force, which is higher than the rest, is found alongside the total sum of the forces, i.e., Equation (3) per se. Note that the sign of each term in the equation (+ve or −ve) is also added to the graphs.

Regarding particle inertia and fluid pressure gradient presented in Figure 16a and Figure 16b, respectively, they are closely identical. The significance of these two terms is spotted in the four phases of the circulating loop: acceleration phase in the impeller vicinity, the start of the upward movement near the wall, the second phase of the upward flow, and the end phase on top of the impeller. The values are around 1000 and $-1000\ N/m^3$, which is three times less than lift force effect.

The virtual mass force (added mass) shown in Figure 16c has no contribution to the domain, as the map is almost nil everywhere. This phenomenon is expected, especially for a system with microparticle size and density that is highly close to the carrier fluid.

As for the lift force depicted in Figure 16d, it is dominant in the impeller and wall regions, where vorticity and radial slip velocity act mainly. Note that the lift term could be highly approximated, since the tangential component is unknown; this leads to the approximation of the vorticity term and eventually only the axial lift force is evaluated. In addition, there is no information on the rotation of microparticles, i.e., particle angular velocity, which is impossible to measure using PIV. This information would further contribute to the lift force (Magnus force [69]). The effect of lift and added mass is often ignored and reported to have no considerable contribution to solid–liquid hydrodynamics in stirred tanks, with a positive constant coefficient used, which is C_L = 0.5, and the lift force is much smaller than the drag force [62,74,75]. This coefficient value is valid for free-slip spheres, but likely inapplicable for no-slip surfaces, as the lift generation mechanisms are fundamentally different [76]. Moreover, Derksen [69] mentioned that the flow in a stirred tank is very inhomogeneous, making it difficult to estimate a priori if forces, such as lift, play an important role. That being said, the assessed lift force, using the Saffman coefficient C_L, is three times higher than that of particle inertia and fluid pressure gradient, varying between -2000 and $3000\ N/m^3$.

On the other hand, the estimated drag force is 3–5 times higher than that of the lift force, as can be seen in Figure 16e. This effect was noticed by Montante et al. [40], but with one order of magnitude higher than the lift force. Note that the authors estimated the drag force using the Schiller and Naumann standard base drag model [77], which was in turn modified by adapting the average of Equation (1). For that reason, and since the particle Reynolds number in this work is $Re_p < 3$ (Figure A4 in Appendix A), the choice of Oseen's drag coefficient is adapted [73] instead of Schiller and Naumann (for $Re_p < 1000$). The main regions of drag are in the impeller region and near the wall, where the high axial slip velocity dominates, ranging between $-10{,}000$ and $10{,}000\ N/m^3$.

The total sum of the forces of Equation (3) in the axial direction is finally presented in Figure 16f. Noticeably, the sum is far from nil in the impeller discharge and the wall region, where turbulent dispersion forces and wall interactions are missing from the equation, which are important for modeling multiphase flows, and, hence, the evaluated drag force prevails, whereas in the bulk of the tank, the sum varies around zero and the equation is satisfied. For flows near the wall region, Sommerfeld et al. [78] reported that a drag enhancement may occur in that region and another study by Shi and Rzehak [79] found that a wall-lift force effect was presented and directed away from the wall. It is important to bear in mind that the equation remains a tentative approximation, as the absence of data on the tangential term, as well as the hypothesis of steady flow, further contribute to the mismatches. Montante et al. [40] also reported the same phenomenon in their experimental attempt, also stating that the scalar Eulerian information was adopted for the estimate of Lagrangian terms.

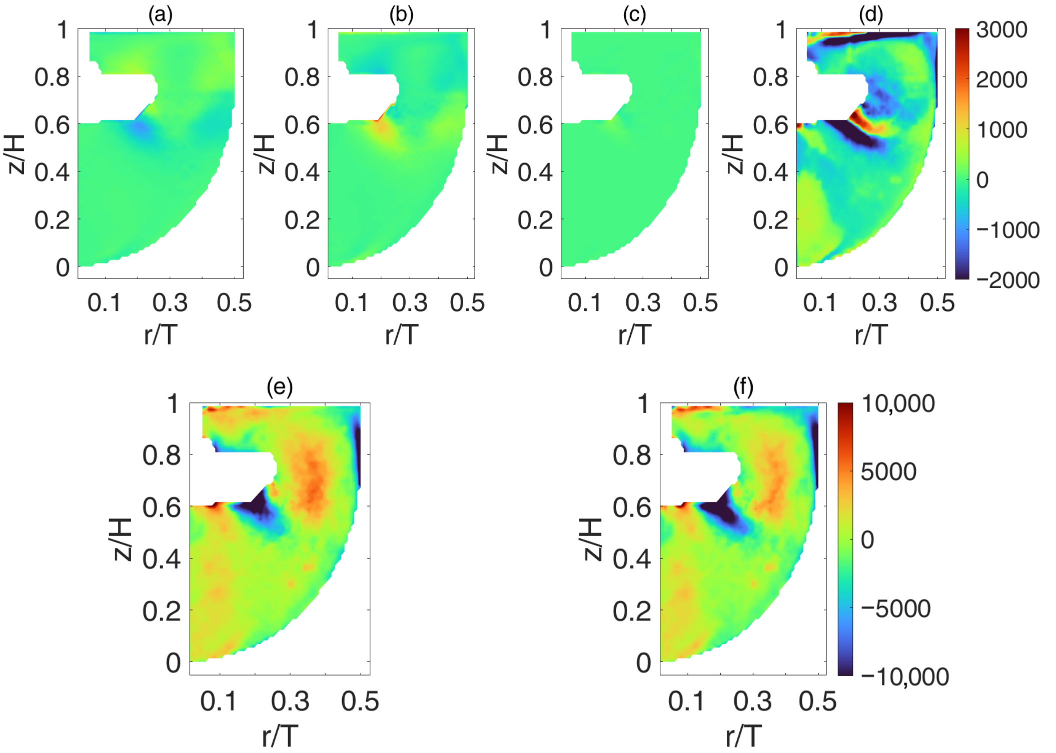

Figure 16. Contour plot of the axial force balance terms and the total sum of Equation (3) for α_p = 0.5 v%. 1st row: Unified scale/color-bar (**a**) inertia (**b**), pressure gradient (**c**), added mass (**d**), lift force. 2nd row: Unified scale/color-bar (**e**) drag force (**f**), total sum of Equation (3). The associated sign of each term (−ve or +ve) inside the balance equation is embedded within the contour plot. Color-bar: N/m^3.

Drag models have been extensively studied in the literature and embedded in computational tools, where it has been proven necessary to include the effect of turbulence on the modeling of drag force in stirred tanks [80]. The appreciable effect of turbulence on the mean drag force resulted in various correlations that depend on the characteristic time and length scales of the domain. The review by Balachandar and Eaton [81] indicates that multiple mechanisms operate and various phenomena emerge under particular conditions; nevertheless, a full comprehensive understanding has not yet been reached. Equations (1) and (2) are examples, and several others can be found in the review by Shah et al. [80]. Since PIV resolution cannot provide information on the Kolmogorov scales, the use of some empirical drag models is only limited to the mean dissipation from power number equation, and, thus, only averaged values are resolved instead of local maps, as approached by Montante et al. [40].

The debate on which correlation adequately fits the slip data could be rather treated with CFD as a future endeavor, as approached by Sardeshpande et al. [61]. Since the ratio of $U_s/U_t > 10$ in the impeller discharge zone, it is important to pay attention to the turbulence intensity quantified there. Recently, Shi and Rzehak [82] highlighted that the use of the drag modification factor from Lane et al. (Equation (2)) resulted in a significant impact of the lift force on the results. Hence, for any CFD validation, a complete model is suggested to account for possible effects of lift, virtual mass, turbulent dispersion, and any modified drag force.

4. Conclusions

A dual-camera particle image velocimetry PIV (2D-2C) technique has been used to map the hydrodynamics of microparticles PMMA suspension of $0.1 \leq \alpha_p \leq 0.5$ v% in an axial mixing stirred tank. The tank is a physical analog of the bioreactor used to culture stem cells within the imposed configuration [83]. Thus, the system has unique specific properties that match the world of stem cell culture: microparticles of microcarrier size $d_p = 168$ µm and a highly close density between the dispersed and carrier phases $\rho_p/\rho_l \approx 0.96$. The simultaneous measurements of both phases allow one to track the effect of particle loading on mean flow, turbulence, slip velocities, and a tentative evaluation of interfacial forces.

The mean flow remained quasi-invariant with the addition of particles, with a slight 10% shift in momentum between single phase and $\alpha_p = 0.5$ v% of the liquid phase. However, solid-phase velocities were slower than those of single phase and carrier phase at the same concentration $\alpha_p = 0.5$ v% (approximately 20% in the impeller discharge zone). It was also noticed that, for solid phase, mean flow structure (circulating loop) differed between $\alpha_p = 0.1$ v% and 0.5 v%.

Turbulence levels were found to diverge sharply between both phases. In the impeller discharge, liquid-phase turbulent kinetic energy TKE rose modestly (10%) from single phase to $\alpha_p = 0.5$ v%, while the solid-phase TKE fell by 25% in that region, and reached up to 50% at maximum levels. The TKE ratio between particles and liquid phases revealed that for $\alpha_p = 0.1$ v%, particles possess slightly higher turbulence. The ratio then decreased drastically at $\alpha_p = 0.5$ v% so that the liquid-phase turbulence was 50% higher than that of the solid phase. Near the wall, where turbulence levels are low, the radial r.m.s velocities of the solids were approximately 30% higher than those of the liquid phase, but the differences became marginal on the TKE side.

Analysis of the slip velocities showed that the particles lag behind the carrier phase in the impeller stream and deviate faster in the wall region. In addition, the slip velocities increased with the increase in the volume fraction of particles. Comparisons with correlations from the literature indicate good agreement, which confirms the modification of settling velocity due to the turbulence of the liquid phase, especially in the bulk of the tank. In the impeller and wall regions, slip velocities are much higher than in the bulk. Both experimental investigations [40] and numerical simulations [69] proved the extent of the high slip velocities in these regions.

In contrast to CFD tools, slip velocities were used directly to approximately evaluate the force balance equation of the particles. Using the Oseen drag coefficient, the drag force was 3–5 times higher than the lift force. Drag and lift forces were dominant in the impeller discharge and wall regions, where slip velocities are high. In the tank bulk, the tentative force balance of the particles is approximately satisfied; i.e., the sum of forces varied around zero. The review by Balachandar and Eaton [81] demonstrated that drag, lift and turbulent dispersion all vary with local strain and vortex topology. Hence, a CFD approach is necessary to compare with the present maps, by adjusting and modifying drag–lift–dispersion models [61]. This will be the next step within this research group in developing and validating further insights into the hydrodynamics for this type of stirred tank including angle-resolved measurements using a high-speed camera to enable direct comparison with the present time-averaged fields.

Supplementary Materials: The following supporting information can be downloaded at: https://www.mdpi.com/article/10.3390/fluids11010017/s1, Figure S1: Back-side of the tank, opposite to camera view. Dip tubes (sensors analogue) are highlighted; Figure S2: Tank under N = 150 rpm with PMMA particles and laser on. Video S1: A video of the tank under N = 150 rpm with PMMA microparticles. The video (gif format) is captured from the same side of the laser sheet (perpendicular to the camera field).

Author Contributions: Conceptualization, M.M., A.D. and D.T.; methodology, M.M. and A.D.; software, M.M., A.D. and S.C.; validation, M.M., A.D. and D.T.; formal analysis, M.M., A.D., S.C. and D.T.; investigation, M.M., A.D. and S.C.; resources, A.D. and S.C.; data curation, M.M. and A.D.; writing—original draft preparation, M.M.; writing—review and editing, A.D. and D.T.; visualization, M.M. and S.C.; supervision, D.T.; project administration, D.T.; funding acquisition, D.T. All authors have read and agreed to the published version of the manuscript.

Funding: The authors are grateful to the Fonds De La Recherche Scientifique—FNRS for their financial support. “OptiReac4MSC”, Ref: 40003532.

Institutional Review Board Statement: Not applicable.

Informed Consent Statement: Not applicable.

Data Availability Statement: The raw data supporting the conclusions of this article will be made available by the authors on request.

Conflicts of Interest: The authors declare no conflicts of interest.

Abbreviations

The following nomenclature, abbreviations, and Greek letters are used in this manuscript:

IA	Interrogation area
LDV	Laser Doppler Velocimetry
MSC	Mesenchymal stem cell
PIV	Particle image velocimetry
PTV	Particle tracking velocimetry
RI	Refractive index
RIM	Refractive index matching
rms	Root mean square
TKE	Turbulent kinetic energy
α_p	Particle volume fraction, –
ε	Energy dissipation rate, $\mathrm{m}^2/\mathrm{s}^3$
μ	Dynamic viscosity, Pa.s
ρ	Density, kg/m^3
η	Kolmogorov length scale, m
C	Impeller clearance, m
D	Impeller diameter, m
d_p	Particle diameter, m
H	Liquid height, m
k	Turbulent kinetic energy, $\mathrm{m}^2/\mathrm{s}^2$
k^*	Non-dimensional turbulent kinetic energy, –
L	Integral length scale, m
M	Mean velocity magnitude, m/s
M^*	Non-dimensional mean velocity magnitude, –
N	Impeller speed, rpm
T	Tank diameter, m
P	Power input, W
P_0	Power number, –
r	Radial coordinate, m

$\overline{U}$	Mean velocity, m/s
u'	Fluctuating velocity, m/s
V	Fluid volume, m^3
z	Axial coordinate, m
Re	Reynolds number, –
St	Stokes number, –

Appendix A

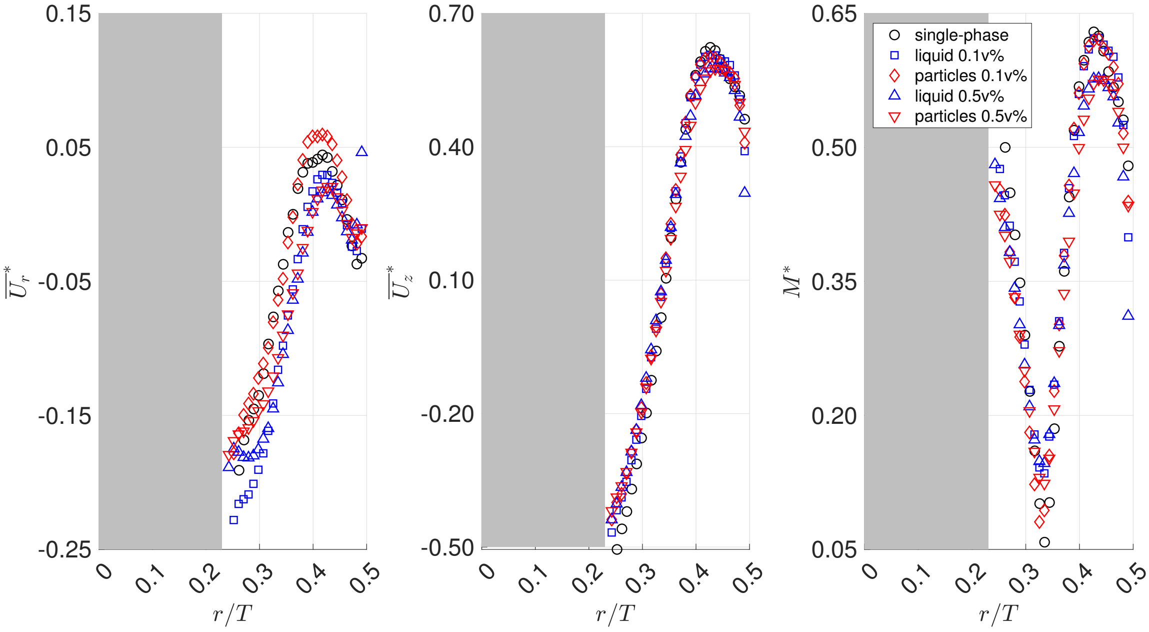

Figure A1. Non-dimensional mean velocity profile plots at z/H = 0.7, scaled by (ND): (**Left**) Mean radial velocity $\overline{U}_r^*$. (**Center**) Mean axial velocity $\overline{U}_z^*$. (**Right**) Mean velocity magnitude M^*. ○: Single phase, □: Liquid phase at α_p = 0.1 v%, ◇: Solid phase at α_p = 0.1 v%, △: Liquid phase at α_p = 0.5 v%, ▽: Solid phase at α_p = 0.5 v%. Gray-shaded area corresponds to impeller; outside the measurement plane.

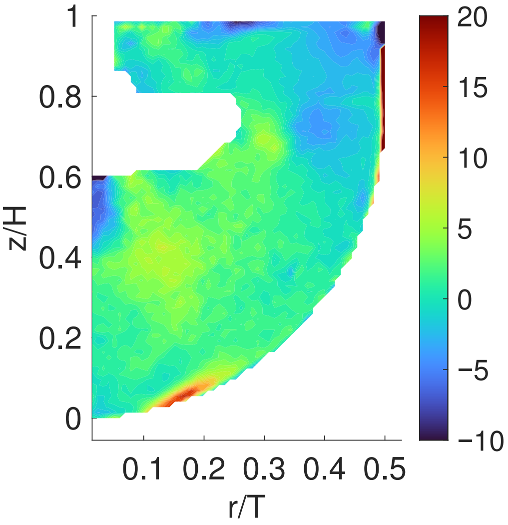

Figure A2. Contour plot of mean/average angle deviations between solids and liquid velocity vectors $\Delta\theta$ in degrees °. solid-phase vectors act as a reference. +ve angle: Particle velocity vector is oriented counter-clock-wise CCW from liquid velocity vectors ↺. −ve angle: Particle velocity vector is oriented clock-wise CW from liquid velocity vectors ↻. Color-bar: $\Delta\theta$ in degrees °.

https://doi.org/10.3390/fluids11010017

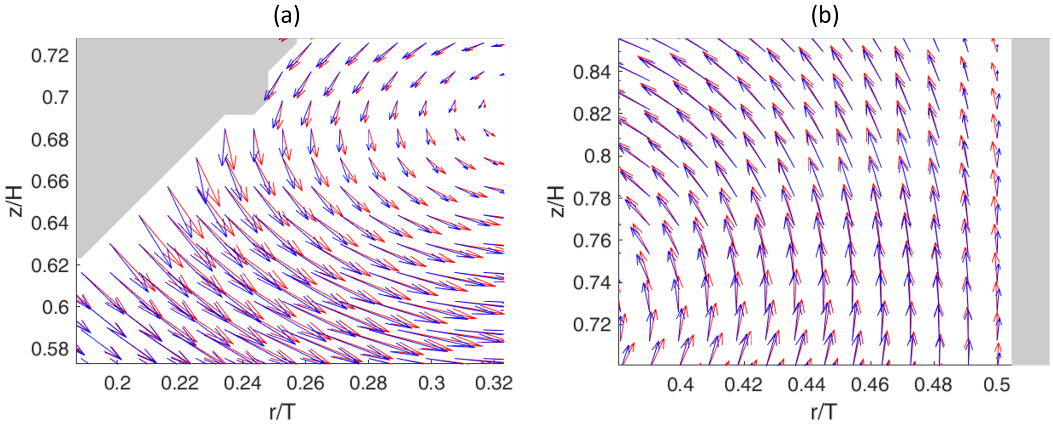

Figure A3. Superimposed mean velocity vectors of solid phase (red) and liquid phase (blue): (**a**) Impeller region, (**b**) near the wall region. Case α_p = 0.5 v%.

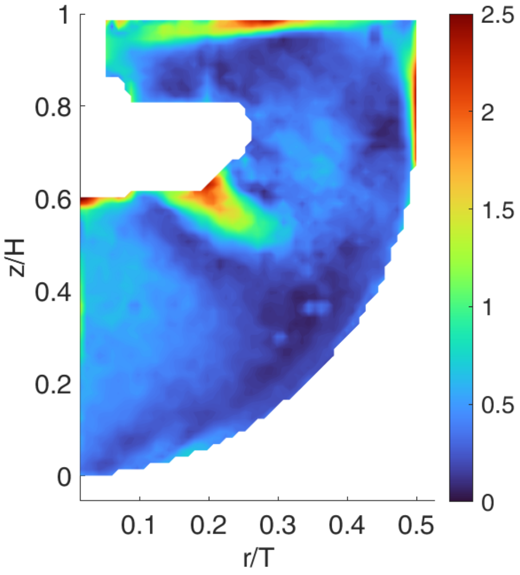

Figure A4. Contour plot of particle Reynolds number Re_p at α_p = 0.5 v%.

References

1. Kumar, V.; Nigam, K. Multiphase fluid flow and heat transfer characteristics in microchannels. *Chem. Eng. Sci.* **2017**, *169*, 34–66. [CrossRef]
2. Zhang, J.s.; Qin, B.m.; Liu, Y.h.; Li, Q.h.; Zuo, X.t.; Wang, C.; Yang, S.f.; Liu, Q. Multiphase flow inside a four-strand continuous casting tundish using three types of ladle shrouds. *J. Iron Steel Res. Int.* **2023**, *30*, 1171–1181. [CrossRef]
3. Zhou, Y.; Yin, D.; Li, Y.; He, J.; Zhang, C. A review of crude oil emulsification and multiphase flows in chemical flooding. *Energy Sci. Eng.* **2023**, *11*, 1484–1500. [CrossRef]
4. Kim, J.; Yu, J.; Lee, S.; Tahmasebi, A.; Jeon, C.H.; Lucas, J. Advances in catalytic hydrogen combustion research: Catalysts, mechanism, kinetics, and reactor designs. *Int. J. Hydrogen Energy* **2021**, *46*, 40073–40104. [CrossRef]
5. Wilson, D.I.; Chew, Y.M.J. Fluid mechanics in food engineering. *Curr. Opin. Food Sci.* **2023**, *51*, 101038. [CrossRef]
6. Balachandar, S. *Fundamentals of Dispersed Multiphase Flows*; Cambridge University Press: Cambridge, UK, 2024.
7. Prosperetti, A.; Tryggvason, G. *Computational Methods for Multiphase Flow*; Cambridge University Press: Cambridge, UK, 2009.
8. Yeoh, G.H.; Tu, J. *Computational Techniques for Multiphase Flows*; Butterworth-Heinemann: Oxford, UK, 2019.
9. Subramaniam, S. Multiphase flows: Rich physics, challenging theory, and big simulations. *Phys. Rev. Fluids* **2020**, *5*, 110520. [CrossRef]
10. Farrar, B.; Samways, A.; Ali, J.; Bruun, H. A computer-based hot-film technique for two-phase flow measurements. *Meas. Sci. Technol.* **1995**, *6*, 1528. [CrossRef]
11. Zenit, R.; Koch, D.L.; Sangani, A.S. Measurements of the average properties of a suspension of bubbles rising in a vertical channel. *J. Fluid Mech.* **2001**, *429*, 307–342. [CrossRef]

12. Ceccio, S.; George, D. A review of electrical impedance techniques for the measurement of multiphase flows. *Fluids Eng.* **1996**, *118*, 391–399. [CrossRef]
13. George, D.L.; Iyer, C.O.; Ceccio, S.L. Measurement of the bubbly flow beneath partial attached cavities using electrical impedance probes. *J. Fluids Eng.* **2000**, *122*, 151–155. [CrossRef]
14. Prasser, H.M.; Scholz, D.; Zippe, C. Bubble size measurement using wire-mesh sensors. *Flow Meas. Instrum.* **2001**, *12*, 299–312. [CrossRef]
15. Tompkins, C.; Prasser, H.M.; Corradini, M. Wire-mesh sensors: A review of methods and uncertainty in multiphase flows relative to other measurement techniques. *Nucl. Eng. Des.* **2018**, *337*, 205–220. [CrossRef]
16. Vejražka, J.; Večeř, M.; Orvalho, S.; Sechet, P.; Ruzicka, M.C.; Cartellier, A. Measurement accuracy of a mono-fiber optical probe in a bubbly flow. *Int. J. Multiph. Flow* **2010**, *36*, 533–548. [CrossRef]
17. Hohermuth, B.; Kramer, M.; Felder, S.; Valero, D. Velocity bias in intrusive gas-liquid flow measurements. *Nat. Commun.* **2021**, *12*, 4123. [CrossRef]
18. Tropea, C.; Yarin, A.L.; Foss, J.F. *Springer Handbook of Experimental Fluid Mechanics*; Springer: Berlin/Heidelberg, Germany, 2007; Volume 1.
19. Fdida, N.; Blaisot, J.B. Drop size distribution measured by imaging: Determination of the measurement volume by the calibration of the point spread function. *Meas. Sci. Technol.* **2009**, *21*, 025501. [CrossRef]
20. Huck, P.; Machicoane, N.; Volk, R. A cost-efficient shadow particle tracking velocimetry setup suitable for tracking small objects in a large volume. *Procedia IUTAM* **2017**, *20*, 175–182. [CrossRef]
21. Erinin, M.A.; Néel, B.; Mazzatenta, M.T.; Duncan, J.H.; Deike, L. Comparison between shadow imaging and in-line holography for measuring droplet size distributions. *Exp. Fluids* **2023**, *64*, 96. [CrossRef]
22. Jasikova, D.; Kotek, M.; Kysela, B.; Sulc, R.; Kopecky, V. Experimental Study of Two-Phase Flow Using Shadowgraphy and IPI Technique. *Int. J. Theor. Appl. Mech.* **2017**, *2*, 107–114.
23. Jamaludin, J.; Zawahir, M.Z.; Rahim, R.A.; Yunus, F.R.M.; Ayob, N.M.N.; Muhammad, S.R.A.; Fadzil, N.S.; Zakaria, Z.; Rahiman, M.H.F. A review of tomography system. *J. Teknol. Sci. Eng.* **2013**, *64*. [CrossRef]
24. Toye, D.; Marchot, P.; Crine, M.; L'Homme, G. Modelling of multiphase flow in packed beds by computer-assisted X-Ray tomography. *Meas. Sci. Technol.* **1996**, *7*, 436. [CrossRef]
25. Heindel, T.T.J. X-Ray flow visualization: Techniques and applications. *J. Fluids Eng.* **2024**, *146*, 010801. [CrossRef]
26. Shaikh, A.; Taha, M.M.; Al-Dahhan, M.H. Phase distribution in Fischer-Tropsch mimicked slurry bubble column via computed tomography. *Chem. Eng. Sci.* **2021**, *231*, 116278. [CrossRef]
27. Salgado, W.; Dam, R.; Salgado, C. Optimization of a flow regime identification system and prediction of volume fractions in three-phase systems using gamma-rays and artificial neural network. *Appl. Radiat. Isot.* **2021**, *169*, 109552. [CrossRef] [PubMed]
28. Cui, Z.; Zhang, Q.; Gao, K.; Xia, Z.; Wang, H. Electrical impedance sensors for multi-phase flow measurement: A review. *IEEE Sens. J.* **2021**, *21*, 27252–27267. [CrossRef]
29. Rasel, R.K.; Chowdhury, S.M.; Marashdeh, Q.M.; Teixeira, F.L. Review of selected advances in electrical capacitance volume tomography for multiphase flow monitoring. *Energies* **2022**, *15*, 5285. [CrossRef]
30. Ren, S.; Dong, F. Interface and permittivity simultaneous reconstruction in electrical capacitance tomography based on boundary and finite-elements coupling method. *Philos. Trans. R. Soc. A Math. Phys. Eng. Sci.* **2016**, *374*, 20150333. [CrossRef]
31. Yang, W. Design of electrical capacitance tomography sensors. *Meas. Sci. Technol.* **2010**, *21*, 042001. [CrossRef]
32. Kiger, K.; Pan, C. PIV technique for the simultaneous measurement of dilute two-phase flows. *J. Fluids Eng.* **2000**, *122*, 811–818. [CrossRef]
33. Kosiwczuk, W.; Cessou, A.; Trinite, M.; Lecordier, B. Simultaneous velocity field measurements in two-phase flows for turbulent mixing of sprays by means of two-phase PIV. *Exp. Fluids* **2005**, *39*, 895–908. [CrossRef]
34. Rottenkolber, G.; Gindele, J.; Raposo, J.; Dullenkopf, K.; Hentschel, W.; Wittig, S.; Spicher, U.; Merzkirch, W. Spray analysis of a gasoline direct injector by means of two-phase PIV. *Exp. Fluids* **2002**, *32*, 710–721. [CrossRef]
35. Borowsky, J.; Wei, T. Simultaneous velocimetry/accelerometry measurements in a turbulent two-phase pipe flow. *Exp. Fluids* **2006**, *41*, 13–20. [CrossRef]
36. Ohmoto, T.; Une, H.; Adachi, K. A Fundamental Study on the Interaction between Driftwood and Free-Surface Flow in an Open Channel. In Proceedings of the International Conference on Civil, Structural and Transportation Engineering, Niagara Falls, ON, Canada, 5–7 June 2022.
37. Shaffer, F.; Ibarra, E.; Savaş, Ö. Visualization of submerged turbulent jets using particle tracking velocimetry. *J. Vis.* **2021**, *24*, 699–710. [CrossRef]
38. Zhang, M.; Xu, M.; Hung, D.L. Simultaneous two-phase flow measurement of spray mixing process by means of high-speed two-color PIV. *Meas. Sci. Technol.* **2014**, *25*, 095204. [CrossRef]
39. Elhimer, M.; Praud, O.; Marchal, M.; Cazin, S.; Bazile, R. Simultaneous PIV/PTV velocimetry technique in a turbulent particle-laden flow. *J. Vis.* **2017**, *20*, 289–304. [CrossRef]

40. Montante, G.; Paglianti, A.; Magelli, F. Analysis of dilute solid–liquid suspensions in turbulent stirred tanks. *Chem. Eng. Res. Des.* **2012**, *90*, 1448–1456. [CrossRef]
41. Villafañe, L.; Aliseda, A.; Ceccio, S.; DiMarco, P.; Machicoane, N.; Heindel, T.J. 50 Years of International Journal of Multiphase Flow: Experimental Methods for Dispersed Multiphase Flows. *Int. J. Multiph. Flow* **2025**, *189*, 105239. [CrossRef]
42. Micheletti, M.; Yianneskis, M. Study of fluid velocity characteristics in stirred solid-liquid suspensions with a refractive index matching technique. *Proc. Inst. Mech. Eng. Part E J. Process Mech. Eng.* **2004**, *218*, 191–204. [CrossRef]
43. Madani, M.; Delafosse, A.; Calvo, S.; Toye, D. RIM-PIV Measurements of Solid–Liquid Flow in a Stirred Tank Used for Mesenchymal Stem Cell Culture. *Fluids* **2025**, *10*, 272. [CrossRef]
44. Virdung, T.; Rasmuson, A. Solid-liquid flow at dilute concentrations in an axially stirred vessel investigated using particle image velocimetry. *Chem. Eng. Commun.* **2007**, *195*, 18–34. [CrossRef]
45. Unadkat, H.; Rielly, C.D.; Hargrave, G.K.; Nagy, Z.K. Application of fluorescent PIV and digital image analysis to measure turbulence properties of solid–liquid stirred suspensions. *Chem. Eng. Res. Des.* **2009**, *87*, 573–586. [CrossRef]
46. Khalitov, D.; Longmire, E.K. Simultaneous two-phase PIV by two-parameter phase discrimination. *Exp. Fluids* **2002**, *32*, 252–268. [CrossRef]
47. Sommer, A.E.; Rox, H.; Shi, P.; Eckert, K.; Rzehak, R. Solid-liquid flow in stirred tanks:"CFD-grade" experimental investigation. *Chem. Eng. Sci.* **2021**, *245*, 116743. [CrossRef]
48. Nouri, J.; Whitelaw, J. Particle velocity characteristics of dilute to moderately dense suspension flows in stirred reactors. *Int. J. Multiph. Flow* **1992**, *18*, 21–33. [CrossRef]
49. Guiraud, P.; Costes, J.; Bertrand, J. Local measurements of fluid and particle velocities in a stirred suspension. *Chem. Eng. J.* **1997**, *68*, 75–86. [CrossRef]
50. Loubière, C.; Delafosse, A.; Guedon, E.; Chevalot, I.; Toye, D.; Olmos, E. Dimensional analysis and CFD simulations of microcarrier 'just-suspended'state in mesenchymal stromal cells bioreactors. *Chem. Eng. Sci.* **2019**, *203*, 464–474. [CrossRef]
51. Delafosse, A.; Loubière, C.; Calvo, S.; Toye, D.; Olmos, E. Solid-liquid suspension of microcarriers in stirred tank bioreactor–experimental and numerical analysis. *Chem. Eng. Sci.* **2018**, *180*, 52–63. [CrossRef]
52. Stamhuis, E.; Thielicke, W. PIVlab–towards user-friendly, affordable and accurate digital particle image velocimetry in MATLAB. *J. Open Res. Softw.* **2014**, *2*, 30.
53. Thielicke, W.; Sonntag, R. Particle Image Velocimetry for MATLAB: Accuracy and enhanced algorithms in PIVlab. *J. Open Res. Softw.* **2021**, *9*, 12. [CrossRef]
54. Stanier, S.A.; Blaber, J.; Take, W.A.; White, D. Improved image-based deformation measurement for geotechnical applications. *Can. Geotech. J.* **2016**, *53*, 727–739. [CrossRef]
55. Sarno, L.; Carravetta, A.; Tai, Y.C.; Martino, R.; Papa, M.; Kuo, C.Y. Measuring the velocity fields of granular flows–Employment of a multi-pass two-dimensional particle image velocimetry (2D-PIV) approach. *Adv. Powder Technol.* **2018**, *29*, 3107–3123. [CrossRef]
56. Ly, S.; Rubenchik, A.M.; Khairallah, S.A.; Guss, G.; Matthews, M.J. Metal vapor micro-jet controls material redistribution in laser powder bed fusion additive manufacturing. *Sci. Rep.* **2017**, *7*, 4085. [CrossRef]
57. Arya, U.; Peterson, W.; Sadeghi, F.; Meinel, A.; Grillenberger, H. Investigation of oil flow in a ball bearing using Bubble Image Velocimetry and CFD modeling. *Tribol. Int.* **2023**, *177*, 107968. [CrossRef]
58. Escudié, R.; Liné, A. Experimental analysis of hydrodynamics in a radially agitated tank. *AIChE J.* **2003**, *49*, 585–603. [CrossRef]
59. Sheng, J.; Meng, H.; Fox, R. A large eddy PIV method for turbulence dissipation rate estimation. *Chem. Eng. Sci.* **2000**, *55*, 4423–4434. [CrossRef]
60. Khan, F.; Rielly, C.; Brown, D. Angle-resolved stereo-PIV measurements close to a down-pumping pitched-blade turbine. *Chem. Eng. Sci.* **2006**, *61*, 2799–2806. [CrossRef]
61. Sardeshpande, M.V.; Juvekar, V.; Ranade, V.V. Solid suspension in stirred tanks: UVP measurements and CFD simulations. *Can. J. Chem. Eng.* **2011**, *89*, 1112–1121. [CrossRef]
62. Ljungqvist, M.; Rasmuson, A. Numerical simulation of the two-phase flow in an axially stirred vessel. *Chem. Eng. Res. Des.* **2001**, *79*, 533–546. [CrossRef]
63. Ljungqvist, M.; Rasmuson, A. The two-phase flow in an axially stirred vessel investigated using phase-Doppler anemometry. *Can. J. Chem. Eng.* **2004**, *82*, 275–288. [CrossRef]
64. Guiraud, P.; Costes, J.; Bertrand, J.; Bousquet, J. Local measurements of liquid and solid velocities and of particle sizes in stirred suspensions with a phase Doppler particle analyser. In *Fluid Mechanics of Mixing: Modelling, Operations and Experimental Techniques*; Springer: Berlin/Heidelberg, Germany, 1992; pp. 145–152.
65. Pinelli, D.; Nocentini, M.; Magelli, F. Solids distribution in stirred slurry reactors: Influence of some mixer configurations and limits to the applicability of a simple model for predictions. *Chem. Eng. Commun.* **2001**, *188*, 91–107. [CrossRef]
66. Fajner, D.; Pinelli, D.; Ghadge, R.; Montante, G.; Paglianti, A.; Magelli, F. Solids distribution and rising velocity of buoyant solid particles in a vessel stirred with multiple impellers. *Chem. Eng. Sci.* **2008**, *63*, 5876–5882. [CrossRef]

67. Lane, G.; Schwarz, M.; Evans, G.M. Numerical modelling of gas–liquid flow in stirred tanks. *Chem. Eng. Sci.* **2005**, *60*, 2203–2214. [CrossRef]
68. Chéron, J.; Loubière, C.; Delaunay, S.; Guezennec, A.G.; Olmos, E. CFD numerical simulation of particle suspension and hydromechanical stress in various designs of multi-stage bioleaching reactors. *Hydrometallurgy* **2020**, *197*, 105490. [CrossRef]
69. Derksen, J. Numerical simulation of solids suspension in a stirred tank. *AIChE J.* **2003**, *49*, 2700–2714. [CrossRef]
70. Brucato, A.; Grisafi, F.; Montante, G. Particle drag coefficients in turbulent fluids. *Chem. Eng. Sci.* **1998**, *53*, 3295–3314. [CrossRef]
71. Hinze, J.O. *Turbulence*, 2nd ed.; McGraw-Hill: New York, NY, USA, 1975.
72. Crowe, C.; Schwarzkopf, J.; Sommerfeld, M.; Tsuji, Y. *Multiphase Flows with Droplets and Particles*, 2nd ed.; Taylor & Francis: Abingdon, UK, 2011.
73. Sobieski, W. Drag coefficient in solid–fluid system modeling with the Eulerian multiphase model. *Dry. Technol.* **2010**, *29*, 111–125. [CrossRef]
74. Ochieng, A.; Lewis, A.E. Nickel solids concentration distribution in a stirred tank. *Miner. Eng.* **2006**, *19*, 180–189. [CrossRef]
75. Khopkar, A.; Rammohan, A.; Ranade, V.; Dudukovic, M. Gas–liquid flow generated by a Rushton turbine in stirred vessel: CARPT/CT measurements and CFD simulations. *Chem. Eng. Sci.* **2005**, *60*, 2215–2229. [CrossRef]
76. Legendre, D.; Magnaudet, J. The lift force on a spherical bubble in a viscous linear shear flow. *J. Fluid Mech.* **1998**, *368*, 81–126. [CrossRef]
77. Schiller, V.L. Uber die grundlegenden Berechnungen bei der Schwerkraftaufbereitung. *Z. Vereines Dtsch. Inge.* **1933**, *77*, 318–321.
78. Sommerfeld, M. *Best Practice Guidelines for Computational Fluid Dynamics of Dispersed Multiphase Flows*; Ercoftac: London, UK, 2008.
79. Shi, P.; Rzehak, R. Lift forces on solid spherical particles in wall-bounded flows. *Chem. Eng. Sci.* **2020**, *211*, 115264. [CrossRef]
80. Raja Ehsan Shah, R.S.S.; Sajjadi, B.; Abdul Raman, A.A.; Ibrahim, S. Solid-liquid mixing analysis in stirred vessels. *Rev. Chem. Eng.* **2015**, *31*, 119–147. [CrossRef]
81. Balachandar, S.; Eaton, J.K. Turbulent dispersed multiphase flow. *Annu. Rev. Fluid Mech.* **2010**, *42*, 111–133. [CrossRef]
82. Shi, P.; Rzehak, R. Solid-liquid flow in stirred tanks: Euler-Euler/RANS modeling. *Chem. Eng. Sci.* **2020**, *227*, 115875. [CrossRef]
83. Sion, C.; Ghannoum, D.; Ebel, B.; Gallo, F.; de Isla, N.; Guedon, E.; Chevalot, I.; Olmos, E. A new perfusion mode of culture for WJ-MSCs expansion in a stirred and online monitored bioreactor. *Biotechnol. Bioeng.* **2021**, *118*, 4453–4464. [CrossRef]

https://doi.org/10.3390/fluids11010017